Revision 3

Contrasting magma compositions between Cu and Au mineralized granodiorite intrusions in the Tongling ore district in South China using apatite chemical composition and Sr-Nd isotopes

Li-Chuan Pan[a], Rui-Zhong Hu[a,b]*, Abiola Oyebamiji[a], Hong-Yuan Wu[c], Jin-Wei Li[a], Jin-Xiang Li[a]

[a] State Key Laboratory of Ore Deposit Geochemistry, Institute of Geochemistry, Chinese Academy of Sciences, Guiyang 550081, China

[b] College of Earth and Planetary Sciences, University of Chinese Academy of Sciences, Beijing 100049, China

[c] The Bureau of Geology and 321 Mineral Exploration Team of Anhui Province, Tongling, 244000, China

*Corresponding author: Tel, +86-851-5891962; Fax, +86-851-5891664
e-mail, huruizhong@vip.gyig.ac.cn

Abstract

Identifying magma fertility is an important task in ore genesis research. In this paper, we use apatite chemistry and Sr-Nd isotopes for such a study. The apatite crystals are from four Cretaceous coeval granodiorite intrusions with different styles of hydrothermal mineralization in the Tongling ore district, South China. The selected intrusions are Hucun, Dongguashan and Xinwuli, which host both porphyry and skarn Cu deposits, and the Chaoshan, which hosts a skarn Au deposit. The abundances of apatite major and trace elements, such as Mn, V, Ce, S, F, Cl, and Cu, together with the whole-rock compositions, are used to decipher the oxidation states, volatile compositions, and Cu fertility of the parental magmas. The apatite Sr-Nd isotope compositions are used as tracers for the magma sources. The results show that (1) the parental magma of the Au-mineralized intrusion is less oxidized and has higher S-Cl contents than those of the Cu-mineralized intrusions, and (2) the proportion of mantle-derived melt is much higher in the former than in the latter. The results also reveal that the Cu-mineralized intrusions have highly variable apatite Cu-Cl-S compositions. Specifically, the Xinwuli intrusion has much higher Cu but lower Cl-S contents in apatite than other two intrusions, indicating that a Cu-rich magma is not universally required for the formation of hydrothermal Cu deposits. This study demonstrates that apatite is a robust petrogenetic and metallogenic indicator for porphyry and skarn -type Cu-Au ore deposits.

Keywords: Apatite; Magma oxidation state; Sr-Nd isotopes; LA-ICP-MS; Cu and Au mineralization

Introduction

Porphyry and skarn-type Cu and Au deposits are important resources of these metals in the world (Cooke et al., 2005; Meinert et al., 2005; Sillitoe, 2010). In light of their similar geochemical characteristics as strongly chalcophile elements (Peach et al., 1990), Cu and Au association is common in the porphyry and skarn-mineralized systems (Meinert et al., 2005; Sillitoe, 2010). But Cu and Au could also be mineralized separately in porphyry and skarn deposits, although the ore-related plutons could be closely related in time and space. For example, the Cenozoic porphyries located in the Jinshajiang-Red River metallogenic belt, eastern Tibet can host Cu deposits (i.e., Machangjing and Tongchang) and Au deposits (i.e., Yao'an and Beiya) (Hou et al., 2006; Bi et al., 2009). As a result, there is debate about the fundamental controls on the different styles of mineralization associated with granite plutons, such as hydrothermal Cu versus Au mineralization. A popular view is that highly oxidized magma is required for the formation of a porphyry and skarn Cu or Au ore deposit, because under relatively more oxidized conditions, Cu and Au can be more easily transported by magma to upper crustal levels and become highly concentrated in the ore-forming magmatic fluids (e.g., Ballard et al., 2002; Richards, 2015; Richards and Şengör, 2017). However, a recent study found that the parental magma of an ore-barren granitic pluton in the Ailaoshan region, SW China is as oxidized as those of some porphyry Cu ore deposits in northern Chile (Xu et al., 2019). Moreover, although the consensus is that high metal abundance in magma is favorable to Cu and Au mineralization (Sun et al., 2015), some new data from melt inclusion studies do not show higher metal contents in the parental magmas for the ore-bearing plutons than that for the ore-barren plutons (Lerchbaumer and Audėtat et al., 2013; Zhang and Audétat, 2017).

In the past, whole-rock geochemical data alone were used to determine the oxidation states and metal fertility of granitic pluton but only yielded limited success, mainly due to the fact that whole-rock compositions rarely preserve the original magma compositions, especially those that have experienced pervasive hydrothermal alteration and weathering. Apatite ($Ca_5(PO_4)_3F$) is a common accessory phase and an important sink for halogens and some trace elements in granites. Unlike some the rock-forming minerals in these rocks such as feldspars, biotite, and hornblende,

apatite is much less susceptible to hydrothermal alteration and weathering (Ekstrom, 1972; Ayers and Watson, 1991; Creaser and Gray, 1992). In addition, the fundamental controls on apatite crystallization and composition are well understood, owning to many excellent experimental studies (e.g., Watson, 1979, 1980; Harrison and Watson, 1984; Jahnke, 1984; Pichavant et al., 1992; Wolf and London, 1994, 1995; London et al., 1999). For example, we now know that apatite can crystallize early in some intermediate-felsic magmas based on experimental results (e.g., Harrison and Watson, 1984) and the textural observations of natural samples such as the presence of apatite inclusions enclosed in feldspar, biotite and hornblende in some granodiorites (e.g., Ding et al., 2015; Qian et al., 2019 and this study). The temperature interval of apatite crystallization from granitic magma is relatively short, mainly within 60-100℃after magma begins to saturate with apatite (Piccoli and Candela, 1994; 2002). The concentrations of REE, Sr, Cl, F, S, Eu, and Ce in apatite are a function of magma composition, temperature and redox condition (Sha and Chappell, 1999; Tepper and Kuehner, 1999; Belousova et al., 2001, 2002; Piccoli and Candela, 2002; Cao et al., 2012; Miles et al., 2014). For the reasons mentioned above, plus the recent advance in *in-situ* analytical techniques for trace elements and isotopes, apatite is now widely used to study ore genesis associated with magma evolution (e.g., Sha and Chappell, 1999; Imai, 2002, 2004; Tollari et al., 2008; Huang et al., 2018; Sun et al., 2019; Mercer et al., 2020).

In this study, we use the trace elements (measured using LA-ICP-MS) and Sr-Nd isotopes (determined using LA-MC-ICP-MS) of apatite from four granodiorite intrusions in the Tongling ore district, plus complimentary whole-rock data to evaluate the magmatic controls on the different styles of hydrothermal mineralization, i.e., Cu versus Au mineralization in the region. Our new data show significant compositional differences of apatite in the host rocks with the different styles of mineralization. The results from this study confirm that apatite is a robust petrogenetic and metallogenic indicator for porphyry and skarn -type ore systems.

Geological background

The Tongling region is an important ore district of the Middle-Lower Yangtze metallogenic belt that is situated in the northeastern part of the Yangtze block (Fig. 1a). In this region,

Paleozoic–Mesozoic sedimentary rocks overlie Precambrian metamorphic rocks (Deng et al., 2011; Cao et al., 2017). Early-Middle Triassic carbonates are the country rocks of many younger granodiorite plutons with Cu, Au, Fe, and Mo mineralization in the Tongling ore district.

Spatially, the Middle-Lower Yangtze metallogenic belt is close to the continental collision zone between the North China block and the Yangtze block (Fig. 1a). The collision took place in the Middle Triassic, producing series of NE-trending folds and major faults (Xie et al., 2012). From Late Jurassic to Early Cretaceous, the region underwent post-collisional extension, resulting in lithospheric delamination and associated voluminous magmatism (Xu et al., 2002; Wang et al., 2006). Meanwhile, Paleo-Pacific plate was subducting beneath eastern China (Zhou et al., 2006; Li and Li, 2007; Sun et al., 2007). Some granodiorite intrusions emplaced between 150 and 134 Ma in the Tongling region host hydrothermal Cu and Au ore deposits (Fig. 1b, Deng et al., 2011). Four of them are selected for this study. They are the Hucun, Dongguashan and Xinwuli intrusions that host both porphyry- and skarn-type Cu ore deposits, and the Chaoshan intrusion that hosts only skarn-type Au ore deposit (Lu et al., 2007; Yang et al., 2008; Cao et al., 2017; Wang et al., 2018; Liu et al., 2019).

The Au-mineralized intrusion

The Chaoshan intrusion is located ~7 km southeast of the Tongling city. It intrudes Early-Middle Triassic limestones and shales. The exposure of this intrusion measures approximately 0.3 km^2 (Fig. 2a). It is mainly composed of pyroxene diorite that contains ~70% plagioclase, ~10% pyroxene, ~15% hornblende and ~5% biotite. The accessory minerals include apatite and zircon. Apatite occurs mainly as euhedral crystals surrounded by biotites (Fig. 3a–c). Skarns are common in the contacts with limestones. Some of the skarns contain Au mineralization, with an average Au grade of 18.4 g/t (Wang et al., 2008b). Gold mainly occurs as native Au inclusions enclosed in pyrrhotite, pyrite, and arsenopyrite crystals. Pyrrhotite separates from the Au-bearing samples yield a Re-Os isochron age of 141.7 ± 9.9 Ma (Wang et al., 2008a), indistinguishable with the SHRIMP zircon U-Pb age of the associated pyroxene diorite (142.9 ± 1.1 Ma) (Wang et al., 2004). The H-O isotope compositions of fluid inclusions are within the range of magmatic fluids (Yang et al., 2008). The isotope compositions of S, C and O in the

Au-bearing sulfides and gangue minerals such as calcite indicate that these elements are mainly derived from the parental magma of the pyroxene diorite (Wang et al., 2008b).

The Cu-mineralized intrusions

The Hucun intrusion was emplaced into the Carboniferous-Triassic sedimentary strata. It covers an area of 0.35 km^2 (Fig. 2a). This intrusion is dominated by medium- to coarse-grained granodiorite that is composed of ~40% plagioclase, ~25% quartz, ~15% K-feldspar, ~15% hornblende, and ~5% biotite. The accessory minerals are apatite, zircon, and titanite. Apatite mainly occurs as euhedral crystals surrounded by plagioclase and hornblende (Fig. 3d–f). Skarns are present in the contacts with limestones in places. Some exoskarn zones contain Cu mineralization with grades from 0.4–0.8 wt.% Cu (Cao et al., 2017). Porphyry-type Cu mineralization occurs at ~1000 m below the present surface within the intrusion. The ore minerals include chalcopyrite, pyrrhotite, pyrite, and minor molybdenite. SHRIMP zircon U-Pb age of the intrusion is 140.0 ± 2.6 Ma (Xu et al., 2008). The fluid compositions and C-H-O isotopes indicate that the ore-forming fluids were mainly derived from the parental magma of the intrusion (Lu et al., 2007; Cao et al., 2017).

The Dongguashan intrusion is surrounded by the Upper Devonian to Lower Triassic sedimentary country rocks (Fig. 2a). This intrusion is composed of medium- to coarse-grained quartz diorite that is composed of ~60% plagioclase, ~15% quartz, ~15% hornblende, ~5% biotite and ~5% K-feldspar. The accessory minerals include apatite, titanite, and zircon. Apatite mainly occurs as euhedral crystals surrounded by plagioclase (Fig. 3g–i). The zircon U-Pb age of this intrusion is 140.3 ± 2.0 Ma (Wang et al., 2015). Both porphyry- and skarn-type Cu mineralizations, which together contain 0.94 Mt Cu at 1 wt% Cu, occur within the intrusion and in the contacts with limestone in places (Wang et al., 2015). Stratiform orebodies are present in the sedimentary sequence up to 1000m away from the contacts. Fluid inclusion data and H-O-S-Pb isotopes indicate that the ore-forming fluids were primarily derived from the parental magma of the intrusion (Xu et al., 2007; Liu et al., 2019).

The Xinwuli intrusion is situated farther away from the Tongling City than the other selected intrusions described above (Fig. 1b). This intrusion covers an area of nearly 10 km^2. The country

158 rocks are Triassic limestone and dolomitic limestone. The Xinwuli intrusion consists of quartz
159 diorite in the margin and granodiorite in the center (Fig. 2b). This may be a result of multiple
160 pulses from the same magma chamber at depth (Shao et al., 2007). Quartz diorite is medium- to
161 fine-grained. It is composed of ~60% plagioclase, ~15% hornblende, ~10% quartz, ~10% biotite
162 and ~5% K-feldspar. Granodiorite is also medium- to fine-grained. It is composed of ~45%
163 plagioclase, ~25% quartz, ~15% K-feldspar, ~10% hornblende and ~5% biotite. The accessory
164 minerals include apatite, titanite, and zircon. Apatite in this granodiorite intrusion occurs as
165 euhedral crystals surrounded by plagioclase (Fig. 3j–l). Both porphyry- and skarn-type Cu
166 mineralizations are associated with this intrusion in several places. At Fenghuangshan, the
167 skarn-type Cu mineralization is predominant, containing a total 0.40 Mt of Cu with an average ore
168 grade of 1.24 wt.% Cu (Pan and Dong, 1999). The molybdenite Re-Os age is 141.7 ± 0.82 Ma and
169 the zircon U-Pb age of the associated granodiorite is 143.1 ± 1.6 Ma (Li et al., 2014). The C-O-S
170 isotopes of hydrothermal calcite and sulfides from the Fenghuangshan Cu deposit support the
171 interpretation that the ore-forming fluids were mainly derived from the parental magma of the
172 granodiorite intrusion (Wang et al., 2018).

173

174 **Analytical Methods**

175 *Whole-rock compositions*

176 The whole-rock samples used in this study are relatively fresh and do not show significant
177 Cu-Au mineralization. The concentrations of major elements in the selected rocks were
178 determined with fused lithium tetraborate glass pellets using an Axios PW4400 X-ray
179 fluorescence spectrometer at the State Key Laboratory of Ore Deposit Geochemistry, Institute of
180 Geochemistry, Chinese Academy of Sciences in Guiyang (SKLODG). The analytical uncertainty
181 is estimated to be ＜5%. The concentrations of trace elements in the whole rocks were analyzed
182 using a PE DRC-e ICP-MS at the SKLODG. Powdered samples (50 mg) were dissolved using
183 mixtures of HF and HNO_3 in high-pressure polytetrafluoroethylene vessels for 2 d at ~190 ℃. Rh
184 was used to monitor signal drift during the analysis. The detailed analytical procedures are
185 described in Qi et al. (2000). The analytical uncertainty is estimated to be within 10%.

Apatite major elements compositions

Apatite crystals were separated from the samples using standard heavy-liquid and magnetic methods and then mounted and polished in epoxy. Targets suitable for the in situ analysis were chosen using CL and BSE images. The contents of major and minor elements in apatite (n = 123) were determined using a JEOL-1600 electron microprobe at the SKLODG. The analytical conditions were: 25 kV accelerating voltage, 10 nA beam current, and 10 μm beam diameter. The electron beam was oriented perpendicular to the apatite c-axis to minimize the error for F analysis (Stormer et al., 1993; Goldoff et al., 2012). The following natural minerals were used for calibration: kaersutite (Ca, Mn, Na, Al, Si, Fe), tugtupite (Cl), and apatite (P, S, F).

Apatite and zircon trace elements compositions

The concentrations of trace elements in apatite (n = 123) and zircon (n = 73) were measured by in situ LA-ICP-MS at the SKLODG. The LA-ICP-MS system was an Agilent 7500a ICP-MS equipped with a Resonetics RESOLution M-50 ArF-Excimer laser gun (λ = 193 nm, 80 mJ, 10 Hz). The laser ablation spot was 44 μm in diameter. The ablated aerosol was fed to the ICP instrument using He gas. The NIST610 and NIST612 standards were used for calibration. For apatite analysis, the content of Ca was measured using ^{43}Ca and normalized using the concentration determined by electron probe analysis. Off-line data reduction was performed using ICPMSDataCal software from Liu et al. (2008). The detection limits of apatite by LA-ICP-MS are estimated to be < 0.3 ppm for Sm and Gd, and < 0.1 ppm for U, Th, Sr, Zr, Ga, Cu and other REE. The detection limits of zircon by LA-ICP-MS are estimated to be < 0.3 ppm for Sm and Gd, and < 0.1 ppm for U, Th, Sr, Zr, Ga, and other REE.

Apatite Sr-Nd isotopes

In-situ apatite Sr isotope measurements were conducted using a Nu Plasma III MC-ICP-MS (Nu Instruments) instrument equipped with a RESOlution-155 ArF193-nm laser ablation sampling system (Australian Scientific Instruments) at the SKLODG. Apatite was ablated in a mixture of helium (350 ml/min) and nitrogen (2 ml/min) atmosphere using the following parameters: 30 s baseline time, 40 s ablation time, 60–104 μm spot size, 6 Hz repetition rate, and 6 J/cm^2 energy density. The analytical procedure and interference correction are the same as those described in

Ramos et al. (2004) and Gao and Zhou (2013). One in-house standard of a modern-day coral was measured after every five samples, and two apatite standards (AP1 and MAD) were analyzed after every thirty samples. The results were used for quality control. The measured $^{87}Sr/^{86}Sr$ ratio for the apatite standard AP1 was 0.71133 ± 0.00004 ($n = 12$), which was identical to the recommended value (AP1: 0.71136 ± 0.00008, Yang et al., 2014).

In-situ apatite Nd isotope measurements were conducted in the same manner as the Sr isotope analysis. The interference of ^{144}Sm on ^{144}Nd was derived from the ^{147}Sm intensity with a natural $^{144}Sm/^{147}Sm$ ratio of 0.205484 (Isnard et al., 2005). The mass bias factor of Sm was calculated from the measured isotopic ratio of $^{147}Sm/^{149}Sm$ and its actual value 1.08680 (Isnard et al., 2005). The mass bias of $^{143}Nd/^{144}Nd$ was normalized to $^{146}Nd/^{144}Nd = 0.7129$ with an exponential law. One apatite standard (Durango) was analyzed after every five samples and the other two apatite standards (AP1 and MAD) were analyzed after every thirty samples. The results were used for quality control. The measured $^{143}Nd/^{144}Nd$ ratio for the apatite standard AP1 was 0.512342 ± 0.000014 ($n = 12$), which was identical to the recommended value (AP1: 0.512352 ± 0.000024) (Yang et al., 2014).

Results

Whole-rock compositions

Whole rock compositions are provided as Supplementary Materials 1. These data indicate that the Hucun, Dongguashan, and Xinwuli intrusions have metaluminous and calc-alkaline compositions (Figs. 4a; b), with a Rittmann index ($\sigma = (Na_2O + K_2O)^2/(SiO_2 - 43)$, units in wt.% Rittmann, 1957; 1962) of 2.37–2.88 and an aluminum saturation index (ASI = molar ratio $Al_2O_3/(CaO+Na_2O+K_2O)$ Zen, 1986; Acosta-Vigil et al., 2003) of 0.74–0.90. The Chaoshan intrusion has a metaluminous and alkaline composition (Figs. 4a; b), with a Rittmann index of 4.54–4.82 and an aluminum saturation index of 0.66–0.68. The intrusive rocks are all characterized by moderate to severe K-Nb,-P-Ti depletions (Fig. 4c) and significant light REE enrichments (Fig. 4d). The Dongguashan, Xinwuli and Hucun intrusions show typical adakite trace element compositions, such as Sr $>$ 400 ppm, Y $<$ 20 ppm, Yb $<$ 2 ppm, $(La/Yb)_N >$

15, and δEu > 0.80 (Defiant and Drummond 1990). In contrast, the Chaoshan intrusion does not show such adakite characteristics.

Apatite major and trace elements

The ideal formula of apatite is simplified as $A_5(XO_4)_3Z$. The A-site usually accommodates Ca^{2+} and other minor or trace cations such as Sr^{2+}, Mn^{2+}, Fe^{2+}, $REE^{3+,2+}$, Y^{3+}, Ga^{2+}, and Na^{+}. The X site is mainly occupied by P^{5+} but can be substituted by other highly charged cations such as V^{5+}, S^{6+}, and C^{4+}. The Z site is occupied by F^{-}, Cl^{-}, and OH^{-}. Based on the F^{-}, Cl^{-}, and OH^{-} compositions, apatite can be subdivided into fluorapatite, chloraptite, and hydroxylapatite. The contents of the major and trace elements in apatite are given as Supplementary Materials 2.

Major elements (Ca-Mn-Na) in the apatite structure

The apatite crystals from the four selected intrusions have similar average CaO contents (54–55 wt.%). The apatite average MnO contents are higher in the Hucun and Chaoshan intrusions (~0.10 wt.%) and are lower in the Xinwuli (0.08 wt.%) and Dongguashan intrusions (0.04 wt.%). The negative correlation between apatite CaO and MnO indicates the equivalent substitution of Ca^{2+} by Mn^{2+} (Fig. 5a) (Pan and Fleet, 2002). The apatite average Na_2O content is the lowest in the Xinwuli intrusion (mostly below the detection limit of EPMA), the highest in the Chaoshan intrusion (0.14 wt.%), and intermediate in the Dongguashan (0.09 wt.%) and Hucun (0.07 wt.%) intrusions. The negative correlation of apatite Na_2O and CaO (Fig. 5b) is related to the following reactions: $Na^{+} + S^{6+} = Ca^{2+} + P^{5+}$ (1), $2Na^{+} = Ca^{2+}$ (2), and $REE^{3+} + Na^{+} = 2Ca^{2+}$ (3) (Rønsbo, 1989; Sha and Chappell, 1999). The positive correlation of apatite Na_2O and SO_3 in the Chaoshan intrusions (Fig. 5c) implies that reaction (1) could be dominant for these apatite crystals. However, the low apatite SO_3 content and the negative correlation of apatite REE and CaO (Fig. 5d) suggest that reactions (3) are more prevalent in the Hucun, Dongguashan, and Xinwuli intrusions.

Major elements (P-S-F-Cl) in the apatite structure

The apatite crystals from the selected four intrusions have similar average P_2O_5 contents (40–41 wt%). The apatite average SO_3 contents are the highest in the Chaoshan intrusion (0.28 wt.%), medium in the Hucun and Dongguashan intrusions (0.17 wt.% and 0.20 wt.%,

269 respectively), and the lowest in the Xinwuli intrusion (<0.16 wt.%). S enters apatite by complex
270 substitutions of $S^{6+} + Si^{4+} = 2P^{5+}$ (4) and reaction (1) (Sha and Chappell, 1999). The positive
271 correlation of apatite CaO and P_2O_5 (Fig. 5e) responds well to reaction (1), while reaction (4)
272 could be negligible because of no Si that was detected by EPMA in apatite. The observed negative
273 correlation of apatite F and Cl (Fig. 5f) supports the reciprocal substitution of these two elements
274 (Pan and Fleet, 2002). Our data show that the Chaoshan intrusion has a relatively high apatite Cl
275 content (average of 0.45 wt.%) and a relatively low apatite F content (average of 2.44 wt.%) and
276 F/Cl ratio (average of 6.2). The apatite crystals from the Xinwuli, Hucun, and Dongguashan
277 intrusions have relatively low Cl contents (averages of 0.11 wt.%, 0.32 wt.%, and 0.33 wt.%,
278 respectively) and relatively high F contents (averages of 2.89 wt.%, 2.76 wt.%, and 2.52 wt.%,
279 correspondingly) and F/Cl ratios (averages of 29.5, 10.6, and 8.2, respectively).

280 Minor elements (REE-Y) in the apatite structure

281 Among the four selected rocks, the apatite total REE content is the highest in the Chaoshan
282 intrusion (average of 7035 ppm), intermediate in the Xinwuli intrusion (average of 6410 ppm) and
283 the Dongguashan intrusion (average of 5469 ppm), and the lowest in the Hucun intrusion (average
284 of 4771 ppm). The magnitude of the REE content in apatite is consistent with that in whole-rock
285 samples. The negative correlation of apatite CaO and REE (Fig. 5d) has implication for the
286 substitution of Ca by REE through reactions that include $2REE^{3+} + [\ ] = 3Ca^{2+}$ (5) and reaction (3)
287 (Pan and Fleet, 2002; Rønsbo, 1989; Sha and Chappell, 1999). Reaction (3) could be important in
288 the Hucun and Chaoshan intrusions because of the positive correlation of REE and Na_2O (Fig. 5g).
289 The chondrite- normalized REE patterns of apatite from the four selected intrusions (Fig. 6) show
290 light REE enrichments relative to heavy REE and a significantly negative Eu anomaly (0.3–0.6).
291 Apatite crystals from the Chaoshan and Xinwuli intrusions have higher Y contents (averages of
292 482 and 413 ppm, respectively) than those from the Hucun and Dongguashan intrusions (averages
293 of 236 and 268 ppm, respectively). The observed positive correlation of apatite Y and REE (Fig.
294 5h) hints the similar partitioning behavior of these two elements as the substitute of Ca in apatite.

295 Trace elements (Sr-Th-U) in the apatite structure

296 Apatite is a relatively Sr-, Th-, and U-rich mineral (Belousova, et al., 2002; Chu et al., 2009).

297 The apatite average Sr contents are identical in the Chaoshan, Hucun, and Xinwuli intrusions
298 (averages of 720, 751, and 714 ppm respectively), but are much lower in the Dongguashan
299 intrusion (343 ppm). The apatite from the Xinwuli intrusion has higher Th and U contents
300 (averages of 116 and 34 ppm, respectively). Lower contents of Th (averages of 30, 22, and 20
301 ppm) and U (averages of 8.9, 7.0, and 5.9 ppm) are observed in apatite from the Chaoshan,
302 Dongguashan, and Hucun intrusions, respectively.

303 Trace elements (Ga-V-Cu-Cr) in the apatite structure

304 These four elements in apatite are considered to be potential monitors of magma composition
305 and oxidation state (Sha and Chappell, 1999; Mao et al., 2016; Sun et al., 2019). Thus, we
306 determined the concentration variations of these elements in our apatite samples. The data show
307 that apatite from the Chaoshan intrusion contains more Ga (average of 20 ppm) than that from the
308 other three intrusions (14–17 ppm). The apatite average V content is higher in the Chaoshan and
309 Xinwuli intrusions (~17 ppm) than that in the Hucun (8.7 ppm) and Dongguashan (11 ppm)
310 intrusions. The apatite Cu content is an order of magnitude lower in the Hucun, Dongguashan, and
311 Chaoshan intrusions (＜0.5 ppm) than that in the Xinwuli intrusion (average of 4.2 ppm). The
312 apatite crystals from these four intrusions have similar average Cr content, ranging from 1.5 ppm
313 to 1.6 ppm.

314

315 *Apatite Sr-Nd isotopes*

316 The in-situ Sr-Nd isotopic data of apatite are provided as Supplementary Materials 3. Apatite
317 from the Chaoshan intrusion has $^{87}Sr/^{86}Sr$ ratios from 0.70638 to 0.70683 and εNd(0) values from
318 −11.6 to −8.3. Overall, apatite from the Hucun intrusion has slightly higher $(^{87}Sr/^{86}Sr)_i$ ratios
319 (0.70718 to 0.70812) and lower εNd(0) values (−15.1 to −8.6). Apatite from the Xinwuli and
320 Dongguashan intrusions has the highest ($^{87}Sr/^{86}Sr$) ratios (0.70820 to 0.70895 and 0.70802 to
321 0.71091, respectively) and the lowest εNd(0) values (−16.3 to −10.8 and −16.6 to −12.1,
322 respectively) among the four studied intrusions. The current and initial $^{87}Sr/^{86}Sr$ ratios of apatite
323 are likely very similar because Rb content in the apatite structure is negligible (Sun et al., 2019).

The calculated initial εNd(t) values of apatite based on the previously reported ages for the intrusions are as follow: from −9.9 to −6.6 for Chaoshan, from −13.1 to −6.6 for Hucun, from −14.3 to −8.9 for Xinwuli, and from −14.8 to −10.0 for Dongguashan.

Trace elements of zircon

The average contents of some trace elements in zircon are given as Supplementary Materials 4. High Th/U ratios (>0.1) confirm that the zircon crystals used in this study are all magmatic. The zircon average Ce contents are 76, 20, 31, and 30 ppm in the Chaoshan, Xinwuli, Dongguashan, and Hucun intrusions, respectively. The zircon average Ti contents are 20, 6.3, 5.9 and 3.6 ppm in the Chaoshan, Xinwuli, Dongguashan, and Hucun intrusions, respectively. We calculated the zircon Ce^{4+}/Ce^{3+} ratio using the method proposed by Ballard et al. (2002). The calculated Ce^{4+}/Ce^{3+} ratios of zircon are included in the Supplementary Materials 4, which show that zircon from the Chaoshan intrusion has a lower zircon Ce^{4+}/Ce^{3+} ratio (average of 31) than that from the Dongguashan, Xinwuli, and Hucun intrusions (average ratios 135, 155, and 274, respectively). We estimated the temperature of early magmas using Ti-in-zircon thermometry proposed by Ferry and Watson (2007). The calculated temperatures of magmas are 957 ℃, 815℃, 757℃ and 807℃ in the Chaoshan, Xinwuli, Hucun and Dongguashan intrusions, respectively (Table. 1).

Discussion

Apatite origin

The apatite crystals from all of the four intrusions are interpreted to be of magmatic origin, not hydrothermal or metamorphic origin. The reasons are as follow. Firstly, the chemical compositions, such as the ranges of Mn, Ca, Na, F, Cl, and H_2O contents in the analyzed apatite are generally consistent with those of magmatic origin that occur elsewhere in the world (Piccoli and Candela, 2002) (see Fig. 7). Secondly, hydrothermal apatite commonly has very high Cl exceeding 3.0 wt.% coupled by low F content (Palma et al., 2019), which is likely due to much higher abundance of Cl than F in the parental hydrothermal fluids (Candela, 1986; Warner et al.,

1998). The high-T hydrothermal alteration (e.g., K silicate alteration) may alter apatite composition (Bouzari et al., 2016), resulting in Cl enrichment in the apatite (Palma et al., 2019). However, the apatite crystals from the selected intrusions all have low Cl contents (＜0.75 wt.%). Thirdly, the apatite crystals used in this study all have higher Th (＞10 ppm) and La (＞1000 ppm) contents than typical metamorphic apatite (Th＜10 ppm and La＜1000 ppm, Henrichs et al., 2018). Finally, the interpretation of a magmatic origin for the apatite crystals used in this study is supported by the textural relationships, such as their occurrence as inclusions of euhedral grains enclosed in plagioclase, biotite, and hornblende (Fig. 3), indicating that the apatite crystals could crystallize before the crystallization of the host silicate minerals. Using the method of Harrison and Watson (1984) and whole rock compositions, the calculated apatite saturation temperatures in the studied intrusive rock are＞890 ℃ (Supplementary Materials 1), further supporting a magmatic origin for the apatite crystals in these rocks.

Magmatic oxidation state

The traditional method that uses the whole-rock Fe^{3+}/Fe^{2+} ratio to determine a magmatic oxidation state may be inaccurate owing to the effect of alteration and weathering on the ratio. The compositions of alteration-resistant minerals such as apatite may be more accurate magmatic redox proxies. Many researchers have demonstrated that the variations of Eu, Ce, Mn, V, and Ga in apatite are related to the changes of magmatic oxidation states (e.g., Drake, 1975; Sha and Chappell, 1999; Streck and Dilles, 1998; Imai, 2002, 2004; Boechat et al., 2003; Cao et al., 2012; Sun et al., 2019). Eu^{3+}, Ce^{3+}, Mn^{2+}, V^{5+}, and Ga^{2+} are favored by apatite because Eu^{3+}, Ce^{3+}, Mn^{2+}, and Ga^{2+} can occupy the heptahedral Ca site while V^{5+} can occupy the tetrahedral P site (Piccoli and Candela, 2002). A higher oxygen fugacity increases Eu^{3+}, Ce^{4+}, Ga^{3+}, Mn^{3+}, and V^{5+} at the expense of Eu^{2+}, Ce^{3+}, Ga^{2+}, Mn^{2+}, and V^{4+} in magma, which facilitates the incorporation of Eu and V, rather than Ce, Mn, and Ga into apatite. As a result, the apatite crystallizing from more oxidized magma will contain more Eu and V but less Ga, Mn, and Ce than that crystallizing from less oxidized magma if the concentrations of these elements is constant in the various magmas. However, the use of these proxies to trace magmatic oxidation states requires careful

consideration of elemental partitioning behaviors in different mineral phases coexisting with apatite. For example, feldspar crystallization can remove large amounts of Eu and Sr from the coexisting melt (Ballard et al., 2002; Bi et al., 2002; Buick et al., 2007). The positive correlation of apatite δEu and Sr (Fig. 8a) means that apatite δEu value and Sr content are profoundly affected by feldspar crystallization in the selected intrusions. Similarly, Ga is compatible in feldspar because it can substitute Al (Bedard 2006). The simultaneous decrease of Ga and Sr contents in apatite from the Hucun and Dongguashan intrusions (Fig.8b) indicates that the low Ga content in the apatite crystals may have resulted from feldspar crystallization. Based on this finding, the δEu and Ga content in apatite is not a suitable index to delineate the magmatic oxidation state in the intrusions from this study.

Despite the limitations, some apatite proxies are still useful, including V concentration. Our data reveal that the Chaoshan intrusion has much higher whole-rock V content (＞200 ppm) than the Xinwuli intrusion (＜100 ppm), but apatite from the former intrusion does not have higher V content. Early crystallization of clinopyroxene from the parental magma for the Chaoshan intrusion may explain lower V content than expected in the apatite crystals from this intrusion. Cr is highly compatible in the clinopyroxene structure (e.g., Johnston and Schwab 2004). Thus, this element may be used to track the effect of clinopyroxene crystallization on the compositions of magma and the apatite crystallizing from the fractionated magma. If a decrease of V content in apatite is due to early clinopyroxene crystallization, a decrease of Cr content in apatite should also occur. Nevertheless, no simultaneous reduction of these elemental contents is observed in the apatite crystals from the Chaoshan intrusion (Fig. 8c). Experimental result showed that V, unlike Cr, may behave as an incompatible element in the clinopyroxene structure when the oxidation state of the magmatic system is above the FMQ buffer (Mallmann and O'Neill 2009). This scenario is likely to prevail in the Chaoshan magmatic system, where the estimated magmatic oxygen fugacity is close to FMQ+0.1 (see below). Magnetite is rare in the Chaoshan intrusion. A previous study has shown that the onset of magnetite saturation usually occurs in magma where SiO_2 content reaches 60 wt.% (Jenner et al., 2010). However, the whole-rock SiO_2 content of the Chaoshan intrusion is less than 55 wt.%. This implies that the magnetite in this intrusion can only crystallize in the late stage of magma evolution and thus the chemical composition of apatite that

is an early mineral phase may not be affected by magnetite crystallization. Finally, the low V content in hornblende (253-348 ppm) and clinopyroxene (151-237 ppm) from the Chaoshan intrusion (Tu 2014) suggests that the amount of V removed from the melt via the crystallization of these minerals is limited. In view of the above findings, we infer that the crystallization of other minerals may fail to trigger a significantly downward V content in apatite from the Chaoshan intrusion. The lower V content than expected in apatite from the Chaoshan intrusion is mainly due to the relatively low magmatic oxygen fugacity, which suppresses the incorporation of V into apatite.

The above inferred oxidation states can be further evaluated using the Ce/La ratios of apatite. Ce and La share chemical similarities and are difficult to fractionate during magma evolution, unless some minerals that have greatly discrepant partition coefficients of La and Ce, such as zircon are also crystallizing. Numerous experiments revealed that Ce is much more compatible than La in the zircon structure (Nardi et al., 2013; Rubatto and Hermann 2007). As a result, zircon crystallization may lead to a decrease of Ce/La ratio in the apatite crystallizing from the fractionated magma. Similarly, zircon crystallization may increase the Nd/Yb ratio in the apatite, because Yb is more compatible than Nd in zircon structure (Nardi et al., 2013). However, there is no negative correlation between Ce/La and Nd/Yb in the apatite crystals from the selected four intrusions (Fig. 8d). Since the Ce and La contents of zircon are nearly two orders of magnitude lower than that of coexisting apatite in the samples, it seems that zircon crystallization does not influence the Ce/La ratio of coexisting apatite. The whole-rock Ce/La ratio is uniform in the selected four intrusions (1.88-2.00), but the apatite from the Chaoshan intrusion has a higher Ce/La ratio (average of 1.89) than that from the other three intrusions (average of 1.52- 1.76). This is probably due to the lower oxygen fugacity of the parental magma for the Chaoshan intrusion compared to that of other three intrusions. It follows that the relatively reduced conditions cause the increase of Ce^{3+} at the expense of Ce^{4+} in the melt and facilitate the incorporation of more Ce into apatite in the form of Ce^{3+} to substitute Ca. However, the content of La in apatite is independent of magmatic oxidation state because La^{3+} is the only major ionic form of this element. As a result, the change of oxygen fugacity can not change the efficiency of La replacing Ca in apatite. In view of the above understanding, the higher Ce/La ratio in apatite from the Chaoshan

437 intrusion may indicate a more reduced magma system in this intrusion relative to the other three
438 intrusions.

439 Moreover, a previous study testified that the Mn content in magmatic apatite can be used to
440 estimate the oxygen fugacity of a magmatic system (Miles et al., 2014). The calculated results
441 (Table.1) based on an equation proposed by Miles et al. (2014) manifest that the Chaoshan
442 intrusion formed from a relatively reduced magmatic system (ΔFMQ +0.1), while the Hucun,
443 Dongguashan and Xinwuli intrusions formed from relatively more oxidized magmatic systems (＞
444 ΔFMQ +3).

445 To independently verify this aforementioned findings from apatite redox proxies, we have
446 estimated the magmatic oxygen fugacity using zircon Ce data. The data show that the calculated
447 zircon Ce^{4+}/Ce^{3+} ratios for the Chaoshan intrusion are lower than that for the Dongguashan,
448 Xinwuli, and Hucun intrusions. The zircon data also indicate less oxidized condition for the
449 Chaoshan magmatic system than the other three magmatic systems, consistent with the results
450 from apatite (Fig. 8e).

451 The results from this study indicate that the magma leading to Au mineralization is less
452 oxidized than the magma associated with Cu mineralization. One of the underlying reasons is that
453 the solubility of Au in magma is related to the amount of reduced S (S^{2-}) in the magma, which in
454 turn is related to the oxygen fugacity of the magma (Zajacz et al., 2012). Au can be easily
455 dissolved as a bisulfide complex (such as Au-S-O, AuHS, Au_2S_3, $AuFeS_2$, or AuS(K/Na)) in
456 relatively reduced magma, but it is more difficult to be dissolved in the relatively more oxidized
457 magma (＞ΔNNO+1) because under such more oxidized conditions it tends to occur as less
458 soluble species such as metallic Au or AuO_2 (Botcharnikov et al., 2011; Jégo and Pichavant, 2012;
459 Zajacz et al., 2012). Several experiments have also demonstrated that the solubility of Au in
460 magma rapidly decreases when oxygen fugacity exceeds ΔFMQ +1, whereas the solubility of Cu
461 continues to increase (Bell et al., 2011; Botcharnikov et al., 2011; Jégo and Pichavant, 2012;
462 Zajacz et al., 2012; Li and Audétat, 2013). Among the four selected intrusions, Au could be more
463 abundant in the parental magma for the Chaoshan intrusion because the magma was less oxidized
464 (ΔFMQ+0.1) and could dissolve more Au for the later hydrothermal mineralization, whereas Au

could be barren in the parental magmas for the other three intrusions (Dongguashan, Hucun and Xinwuli) because their parental magmas were highly oxidized (>ΔFMQ+3). This may explain the different metallogenic affinities for the different intrusions from this study.

Magma compositions

Volatile components

During magma solidification, volatile components such as F, Cl, H_2O and S would be gradually exhausted in the melt owing to fluid exsolution or degassing. Hence, the whole-rock composition cannot representatively record the initial volatile contents in magma. Fluid saturation and exsolution may occur at the early stages of magma differentiation in the magma with high initial water content such as ore-forming magma (usually >4%) (Zhu et al., 2018). This prevents the metal loss caused by crystallization of minerals and facilitates metal partitioning into the hydrothermal fluid (Cline and Bodnar, 1991). The parental magma for porphyry Cu deposit could attain massive fluid exsolution during hornblende crystallization (Li et al., 2018). Therefore, hornblende and biotite may not track the initial halogen compositions of magma if they crystallize after massive fluid exsolution. In some dioritic magmatic systems, such as those from this study, apatite can crystallize earlier than hornblende and biotite, as evidenced by the textures (Fig. 3). In these cases, apatite can be used to evaluate the initial halogen and sulfur compositions of the magma (e.g., Boyce et al., 2010; Elkins-Tanton and Grove, 2011).

Our data show that apatite in the Chaoshan intrusion has higher Cl and SO_3 contents but lower F/Cl ratio than apatite in the Hucun, Dongguashan, and Xinwuli intrusions (Fig. 9). The S contents of the parental magmas for these intrusions were estimated using the apatite/melt partition coefficients of Peng et al. (1997) and Parat et al. (2011) and the Cl and F abundances in the magmas were calculated using the apatite/melt partition coefficients of Parat et al. (2011). The results (Table 1) indicate that the Au-mineralized magma contains more Cl and SO_3 and less F than the Cu-mineralized magmas. The solubility of Cu is influenced only slightly by the presence of S and Cl because the dominant Cu species in the melt is $CuO_{0.5}$ (Zajacz et al., 2012). In contrast, the solubility of Au increases significantly with increasing S and Cl contents in the melt (Botcharnikov et al., 2011; Zajacz et al., 2012). Considering this different effect of S and Cl on the

493 solubility of Cu and Au in the melt, the enrichment of magmatic S and Cl plays a more important
494 role in the accumulation of sufficient Au in evolving melt for hydrothermal mineralization. The
495 higher F contents of apatite in these three Cu-mineralized intrusions relative to the Au-mineralized
496 intrusion might be attributed to the input of more crustal components into the parental magmas of
497 the Cu-mineralized intrusions. This is supported by the apatite Sr-Nd isotope (discussed later).
498 Also, the parental magma of the Xinwuli intrusion shows lower Cl and SO_3 contents than that of
499 the Hucun and Dongguashan intrusions.

500 It is generally accepted that Cl shows a strong preference for aqueous solutions relative to F
501 (Candela, 1986; Boudreau and Kruger, 1990). Hydrothermal fluid exsolution can inevitably result
502 in the depletion of Cl relative to F in the coexisting melt. Therefore, an increase in the F/Cl ratio
503 of apatite may be indicative of continuous exsolution of Cl-bearing fluid from magma during
504 apatite crystallization (e.g., Huang et al., 2019). Moreover, crystallization of feldspar will decrease
505 Sr in the residual melt (Bedard, 2006). During this process, apatite crystallizing late will have
506 lower Sr content than that crystallizing earlier. This decreased Sr content closely corresponds to
507 the elevated F/Cl ratios in some apatite crystals, which may be due to Cl-bearing fluid exsolution
508 during progressive crystallization of apatite and feldspar (Fig. 10a). But the degree of fluid
509 exsolution is likely limited as fluid inclusions in apatite are rare. Furthermore, if a large amount of
510 Cl-bearing fluids escaped from magma during apatite crystallization, the mole fractions of
511 hydroxylapatite and chlorapatite in apatite would decrease together, which is not indicated by the
512 data (Fig. 10b).

513 Metal fertility

514 Whole-rock samples from the host intrusions of porphyry and skarn-type Cu deposits
515 commonly contain minor amounts of disseminated hydrothermal chalcopyrite and bornite. As a
516 result, the Cu contents in whole rocks tend to be higher than those in the parental magmas. Thus,
517 the metal contents in some mineral structures is a better proxy to track the parental magma
518 composition. Apatite may contain Cu through substitution of Ca^{2+} by Cu^{2+} (Wang et al., 2016).
519 Although the Cu partition coefficient between apatite and melt remains uncertain, the different
520 ionic radius between Cu^{2+} and Ca^{2+} and the low content of Cu in natural apatite indicates that Cu is

521 likely incompatible in the apatite structure. This incompatibility of Cu signifies that apatite
522 crystallizing at any stage of magma evolution is unable to scavenge a significant fraction of Cu
523 from the melt. However, the contents of Cu in some natural apatite crystals are still high enough to
524 be measured by LA-ICP-MS, providing an useful indicator for Cu fertility in the parental magma.

525 It is widely accepted that the crystallization of major rock-forming minerals such as
526 hornblende, pyroxene, feldspar and biotite do not remove Cu from the parental magma because Cu
527 is highly incompatible in the mineral structures (Bedard, 2006; Le Roux et al., 2015; Hsu et al.,
528 2017; Liu et al., 2015). However, the Cu content in melt and apatite could be strongly controlled
529 by the crystallization of Cu-bearing sulfides or the exsolution of Cu-bearing fluids during apatite
530 crystallization. Crystallization of magmatic sulfides directly from magma will result in a
531 significant decrease of Cu and S in the residual magma, because Cu can be sequestered by many
532 sulfide phases (Jugo and Candela, 1999). The exsolution of Cl-rich fluids from magma will reduce
533 the amount of Cu in the magma because Cu can strongly partition into the fluids as Cl- complexes
534 (Candela and Holland, 1984; Williams-Jones et al., 1995; Webster, 2004). It is currently accepted
535 though, that direct saturation of sulfide from magma is not favorable for Cu and Au mineralization
536 (Richards, 2015; Sun et al., 2015). In fact, sulfide saturation may occur in relatively reduced
537 magma but not in highly oxidized magma (Jugo et al., 2005). For this reason magmatic sulfides
538 (e.g. pyrrite and chalcopyrite) are mainly found in the host rocks of some reduced-type porphyry
539 Cu deposits such as the San Anto (Mexico), Mamut (Malaysia) and San Jorge (Argentina) deposits
540 (fO_2 < FMQ, Rowins 2000). The four intrusions we have studied clearly formed from more
541 oxidized magma (fO_2 > FMQ). The concentrations of S in the parental magmas for these four
542 intrusions, estimated based on apatite S contents (Table 1), are all lower than the value required
543 for pyrite saturation (~1500 ppm) (Moune et al., 2009) and the S solubility in andesitic and
544 rhyolitic melt (~1000 ppm) (Clemente et al., 2004). Sulfide melt inclusions are absent in these
545 intrusions, which may be partly attributed to high magmatic oxygen fugacity. Experimental result
546 has shown that S almost exists in the form of S^{6+} in the oxidized magma (fO_2 > FMQ+2.0). (Jugo
547 et al., 2005). Based on these conditions, we do not expect that there was major magmatic sulfide
548 saturation in the magma types investigated in this study. If a large amount of Cu was extracted by

549 Cl-bearing fluid during apatite crystallization from the parental magmas for these intrusions, a
550 reduced Cu content and similarly decreased Cl content in apatite would be expected. But such
551 correlation is not found (Fig. 11a), implying that the potential large-scale hydrothermal fluid
552 exsolution mainly occurred after apatite crystallization and thus the studied apatite can be used to
553 track the initial Cu contents in the parental magmas.

554 The contents of Cu in apatite from the Cu-mineralized intrusions are dramatically different
555 between them (Fig. 11a; b). Apatite from the Xinwuli intrusion has Cu content ten times higher
556 than apatite from the other two intrusions (Hucun and Dongguashan). The contents of Cu in
557 apatite from the Hucun and Dongguashan intrusions are as low as that from the Chaoshan
558 intrusion which is not related to any Cu mineralization. The reason for the contrasting Cu contents
559 in apatite from the three Cu-mineralized intrusion is elusive, but one possibility is a magma source
560 with different Cu abundance for the different intrusions. Cu-rich magma is considered to be a
561 prerequisite for the formation of porphyry- and skarn-type Cu deposits by some researchers (e.g.,
562 Halter et al., 2005; Core et al., 2006; Stern et al., 2007; Richards, 2009). The results from this
563 study, as well as those from the study of the Bingham deposits (Zhang and Audétat, 2017),
564 indicate that such requirement is not universal. We believe that fluid compositions can play a
565 prominent part in Cu mineralization. The fluids derived from the relatively Cl-rich causative
566 magmas of the Hucun and Dongguashan intrusions are likely to contain more high salinity fluids
567 and thus can transport more Cu as Cl-complexes. This is conducive to the extraction of Cu into the
568 hydrothermal fluid and can lead to Cu mineralization even if the parental magma is not
569 particularly enriched in Cu.

570

571 *Magma mixing*

572 As mentioned above, the apatite major and trace elements reveal significant differences in the
573 redox conditions and chemical compositions between Au-mineralized and Cu-mineralized
574 magmatic systems. These differences may be partly related to mixing of magmas with different
575 proportions of the crust-derived and mantle-derived components. Previous studies have shown that
576 F is high in the crust (Aoki et al., 1981; Gundmundur et al., 1986). Thus, we envisage that higher

F content in apatite from the intrusions related to Cu mineralization relative to that in apatite associated with Au mineralization might result from the higher contribution of the crust-derived components to the parental magmas of these intrusions. The whole-rock Sr-Nd isotope data for the igneous rocks in the Tongling region show that pyroxene diorite such as that of the Chaoshan intrusion generally have lower $(^{87}Sr/^{86}Sr)_i$ ratios and higher εNd(t) value than granodiorite and quartz diorite such as those in the Hucun, Dongguashan, and Xinwuli intrusions (Xie, 2008). However, owing to the possible effect from weathering and alteration on whole-rock Sr-Nd isotope data, more evidence is needed to reach this conclusion. Recently, the values of in-situ apatite $^{87}Sr/^{86}Sr$ and $^{143}Nd/^{144}Nd$ have been accurately detected by LA-MC-ICP-MS (Yang et al., 2014). The advantage of Sr-Nd isotope in apatite as an effective reflection of that in the parental magma is that the early crystallization of apatite could largely avoid the possible isotope fractionation caused by the late crystallization of other minerals. Our apatite results show higher εNd(t) values and lower initial $(^{87}Sr/^{86}Sr)_i$ ratios for the Chaoshan intrusion than the other three intrusions (Fig. 12). The Sr-Nd isotope data are consistent with the interpretation that the parental magma of the Au-mineralized Chaoshan intrusion contains higher amount of mantle-derived materials than those of the other three Cu-mineralized intrusions.

The finding that magma with a larger mantle component is favorable for Au mineralization might be ascribed to Au fertilization in the metasomatized enriched lithospheric mantle. Previous studies have showed that the metasomatized enriched lithospheric mantle such as that in North China and Papua New Guinea could be enriched in Au (Grrifin et al., 2013; Saunders et al., 2018; McInnes et al., 1999). The Au content in the mantle xenoliths collected nearly 300 km away from the Tongling ore district can be more than 6.0 ppb (He et al., 2004), which is higher than the average Au abundance in the continental crust (1.5-3.0 ppb, Taylor 1995; Rudnick and Gao, 2003). Alternatively, the relatively Si-poor magma (SiO_2 < 60 wt.%) due to the mixing with abundant mantle materials will effectively suppress the early crystallization of magnetite and sulfide (Jenner et al., 2010). This is more critical for the mineralization of Au than that of Cu by avoiding the early loss of ore-forming metal from the magma, owing to the higher solid/melt partition coefficient for Au than Cu (Peach et al., 1990; Li et al., 2012; Patten et al., 2013; Mungall et al., 2014). Nevertheless, there is no evidence for the early saturation of sulfide and magnetite in

606 causative magmas of the Cu-mineralized intrusions investigated. Therefore, we favor the addition
607 of different amounts of mantle-derived materials as the reason for the different metallogeny.

608

609 **Conclusions and implications**

610 The results of this study demonstrate that apatite is a good petrogenetic and metallogenic
611 indicator. V-Mn concentrations and Ce/La ratio in apatite can be used to estimate the oxidation
612 states of the parental magma. The concentrations of F, Cl, S, and Cu in apatite can be used to track
613 the volatile compositions and metal fertility of the magma. The apatite Sr-Nd isotopes can be used
614 to evaluate the contributions of crustal and mantle components in the ore-forming magma. The
615 variations of the above proxies in apatite from the selected four intrusions indicate that the magma
616 related to Au mineralization is less oxidized and has higher S and Cl contents plus lower F content
617 than the magma associated with Cu mineralization. We attribute these differences to the possibility
618 that the magma of the Au mineralized system contains higher amounts of mantle-derived
619 components than magma of the Cu mineralized systems, as inferred from the apatite Sr-Nd
620 isotopes. We have also found that apatite from the Cu-mineralized intrusions can have high and
621 low Cu contents with a difference up to ten times, implying that Cu-rich magma is not the
622 prerequisite of porphyry Cu ore formation. Finally, the results from this study indicate that apatite
623 is better than whole rocks to track the compositions of halogen and some trace elements and
624 metals in the parental magma.

625 **Acknowledgments**

626 This study was supported by the Strategic Priority Research Program (B) of the Chinese
627 Academy of Sciences (XDB18000000), “Light of West China” Program of Chinese Academy of
628 Sciences, the National Natural Science Foundation of China (Grant 41703050), and the
629 CAS/SAFEA International Partnership Program for Creative Research Teams (Intraplate
630 Mineralization Research Team; KZZD-EW-TZ-20). We thank Yan-Wen Tang for his assistance in
631 apatite and zircon trace element analysis by LA-ICP-MS, Wen-Qin Zheng and Xiang Li for their
632 support in apatite chemical analysis by EPMA, You-Wei Chen for his help in apatite Sr-Nd

isotopes analysis by LA-MC-ICP-MS and Jing Hu and Shu-Qin Yang for their assistance in the whole-rock chemical analysis by XRF and ICP-MS. We thank the Associate Editor Dr. Antonio Acosta-Vigil, Prof. Thomas Ulrich and an anonymous reviewer for constructive reviews. We are grateful to Dr. Chusi Li of Indiana University and Prof. Thomas Ulrich for their help in manuscript revision.

References

Acosta-Vigil, A., London,D., Morgan VI, G.B., and Dewers, T.A. (2003) Solubility of excess alumina in hydrous granitic melts in equilibrium with peraluminous minerals at 700-800°C and 200 MPa, and applications of the aluminum saturation index. Contributions to Mineralogy and Petrology, 146, 100-119.

Aoki, K., Ishiwaka, K., and Kanisawa, S. (1981) Fluorine geochemistry of basaltic rocks from continental and oceanic regions and petrogenetic application. Contributions to Mineralarogy and Petrology, 78, 53-59.

Ayers, J.C., and Watson, E.B. (1991) Solubility of apatite, monazite, zircon, and rutile in supercritical aqueous fluids with implications for subduction zone geochemistry. Philosophical Transactions of the Royal Society of London, A 335, 365–375.

Ballard, J.R., Palin, J.M., and Campbell, I.H. (2002) Relative oxidation states of magmas inferred from Ce(IV)/Ce(III) in zircon: application to porphyry copper deposits of Northern Chile. Contributions to Mineralogy and Petrology, 144, 347–364.

Bedard, J.H. (2006) Trace element partitioning in plagioclase feldspar. Geochimica et Cosmochimica Acta, 70, 3717-3742.

Bell, A.S., Simon, A. and Guillong, M. (2011) Gold solubility in oxidized and reduced, water-saturated mafic melt: Geochimica et Cosmochimica Acta, 75, 1718-1732.

Belousova, E.A., Walters, S., Griffin, W.L., and O'Reilly, S.Y. (2001) Trace-element signatures of apatites in granitoids from the Mt. Isa Inlier, northwestern Queensland. Australian Journal of Earth Sciences, 48, 603–619.

659 Belousova, E.A., Griffin, W.L., O'Reilly, S.Y., and Fisher, N.I. (2002) Apatite as an indicator
660 mineral for mineral exploration: trace-element composition and their relationship to host rock
661 type. Journal of Geochemical Exploration, 76, 45–69.

662 Bi, X.W., Cornell, D.H., and Hu, R.Z. (2002) REE composition of primary and altered feldspar
663 from the mineralized alteration zone of alkali-rich intrusive rocks, Western Yunnan Province,
664 China. Ore Geology Reviews, 19, 69–78.

665 Bi, X.W., Hu, R.Z., Hanley, J.J., Mungall, J., Peng, J.T., Shang, L.B., Wu, K.X., Suang ,Y., Li,
666 H.L., and Hu, X.Y. (2009) Crystallisation conditions (T, P, fO_2) from mineral chemistry of
667 Cu– and Au–mineralised alkaline intrusions in the Red River–Jinshajiang alkaline igneous
668 belt, western Yunnan Province, China. Mineralogy and Petrology, 96, 43–58.

669 Boechat, C.B., Terra, J., Eon, J.G., Ellis, D.E., and Rossi, A.M. (2003) Reduction by hydrogen of
670 vanadium in vanadate apatite solid solutions. Physical chemistry chemical physics, 5,
671 4290-4298.

672 Botcharnikov, R.E., Linnen, R.L., Wilke, M., Holtz, F., Jugo, P.J., and Berndt, J. (2011) High gold
673 concentrations in sulphide-bearing magma under oxidizing conditions: Nature Geoscience, 4,
674 112-115.

675 Boudreau, A.E., and Kruger, F.J. (1990) Variation in the composition of apatite through the
676 Merensky cyclic unit in the Western Bushveld Complex. Economic Geology, 85, 737-745.

677 Bouzari, F., Hart, C.J.R., Bissig, T., Barker, S. (2016) Hydrothermal alteration revealed by apatite
678 luminescence and chemistry: A potential indicator mineral for exploring covered porphyry
679 copper deposits. Economic Geology, 111, 1397-1410.

680 Boyce, J.W., Liu, Y., Rossman, G.R., Guan, Y. B., Eiler, J.M., Stolper, E.M., and Taylor, L.A.
681 (2010) Lunar apatite with terrestrial volatile abundances. Nature, 466, 466–470.

682 Buick, I.S., Hermann, J., Maas, R., and Gibson, R.L. (2007) The timing of subsolidus
683 hydrothermal alteration in the central zone, Limpopo Belt (South Africa): constraints from
684 titanite U–Pb geochronology and REE partitioning. Lithos, 98, 97–117.

685 Candela, P.A. (1986) Toward a thermodynamic model for the halogens in magmatic systems: an
686 application to melt-vapor-apatite equilibria. Chemical Geology, 57, 289-301.

687 Candela, P.A., and Holland, H.D. (1984) The partitioning of copper and molybdenum between
688 silicate melts and aqueous fluids. Geochimica et Cosmochimica Acta, 48, 373-388.

689 Cao, M.J., Li, G.M., Qin, K.Z., Seitmuratova, E.Y. and Liu, Y.S. (2012) Major and trace element
690 characteristics of apatites in granitoids from Central Kazakhstan: implications for
691 petrogenesis and mineralization. Resource Geology, 62, 63–83.

692 Cao, Y., Zheng, Z., Du, Y., Gao, F., Qin, X., Yang, H., Lu, Y., and Du, Y. (2017) Ore geology and
693 fluid inclusions of the Hucunnan deposit, Tongling, Eastern China: Implications for the
694 separation of copper and molybdenum in skarn deposits. Ore Geology Reviews, 83, 152-173.

695 Chu, M.F., Wang, K.L., Griffin, W.L., Chung, S.L., O'Reilly, S.Y., Pearson, N.J., Iizuka, Y. (2009)
696 Apatite Composition: Tracing Petrogenetic Processes in Transhimalayan Granitoids. Journal
697 of Petrology, 50, 1829-1855.

698 Clemente, B., ScailletC, B., and Pichavant, M. (2004) The solubility of sulphur in hydrous
699 rhyolitic melts. Journal of Petrology, 45, 2171-2196.

700 Cline, J.S., and Bodnar, R.J., (1991) Can economic porphyry copper mineralization be generated
701 by a typical calc-alkaline melt? Journal of Geophysical Research-Solid earth and plants, 96,
702 8113-8126.

703 Creaser, R.A., and Gray, C.M., (1992) Preserved initial 87Sr/86Sr in apatite from altered felsic
704 igneous rocks: a case study from Middle Proterozoic of South Australia. Geochimica et
705 Cosmochimica Acta, 56, 2789–2795.

706 Cook, D.R., Hollings, P., and Walshe, J. (2005) Giant porphyry deposits: Characteristics,
707 distribution, and tectonic controls. Economic Geology, 100, 801-818.

708 Core, D.P., Kesler, S.E., and Essene, E.J. (2006) Unusually Cu-rich magmas associated with giant
709 porphyry copper deposits: Evidence from Bingham, Utah. Geology, 34, 41-44.

710 Defiant, M.J., and Drummond, M.S. (1990) Derivation of some modern arc magmas by melting of
711 young subducted lithosphere. Nature, 347, 662-665.

712 Deng, J., Wang, Q.F., Xiao, C.H., Yang, L.Q., Liu, H., Gong, Q.J. and Zhang, J. (2011)
713 Tectonic-magmatic-metallogenic system, Tongling ore cluster region, Anhui Province, China.
714 International Geology Review, 53, 449-476.

715 Ding, T., Ma, D.S., Lu, J.J.,and Zhang, R.Q. (2015) Apatite in granitoids related to polymetallic
716 mineral deposits in southeastern Hunan Province, Shi‐Hang zone, China: Implications for
717 petrogenesis and metallogenesis. Ore Geology Reviews, 69, 104-117.

718 Drake, M.J. (1975) Oxidation state of europium as an indicator of oxygen fugacity. Geochimica et
719 Cosmochimica Acta, 39, 55–64.

720 Ekstrom, T.K. (1972) The distribution of fluorine among some coexisting minerals. Contributions
721 to Mineralogy and Petrology, 34, 192–200.

722 Elkins-Tanton, L.T., and Grove, T.L. (2011) Water (hydrogen) in the lunar mantle: results from
723 petrology and magma ocean modeling. Earth and Planetary Science Letters, 307, 173–179.

724 Gao, J. F., and Zhou, M. F. (2013). Generation and evolution of siliceous high magnesium basaltic
725 magmas in the formation of the Permian Huangshandong intrusion (Xinjiang, NW
726 China). Lithos, 162, 128-139.

727 Griffin, W.L., Begg, G.C., and O'Reilly, S.Y. (2013) Continental-root control on the genesis of
728 magmatic ore deposits: Nature Geoscience, 6, 905-910.

729 Goldoff, B., Webster, J.D., and Harlov, D.E. (2012) Characterization of fluor-chlorapatites by
730 electron probe microanalysis with a focus on time-dependent intensity variation of halogens.
731 American Mineralogist, 97, 1103-1115.

732 Gundmundur, E., Sigvaldson, E., and Oskarsson, N. (1986) Fluorine in basalts from Iceland.
733 Contributions to Mineralogy and Petrology, 94, 263-271.

734 Halter, W.E., Heinrich C.A., and Pettke T. (2006) Magma evolution and the formation of porphyry
735 Cu-Au ore fluids:Evidence from silicate and sulfide melt inclusions. Mineralium deposita, 39,

845-863.

Harrison, T.M., and Watson, E.B. (1984) The behavior of apatite during crustal anatexis: equilibrium and kinetic consideration. Geochimica et Cosmochimica Acta, 48, 1467–1477.

He, Y., Dong, Z.X., Yue, K.F., Zhang, Z.J., Chen, J.W., and Wang, X. (2004) Content of mantle-derived xenoliths in Eastern China and its metallogenic significance. Geological Review, 50, 418-425.

Henrichs, I.A., O'Sullivan, G., Chew, D.M., Mark, C., Babechuk, M.G., McKenna, C. and Emo, R. (2018) The trace element and U-Pb systematics of metamorphic apatite. Chemical geology, 483, 218-238.

Hou, Z.Q., Zeng, P.S., Gao, Y.F., Du, A.D., and Fu, D.M. (2006) Himalayan Cu–Mo–Au mineralization in the eastern Indo–Asian collision zone: constraints from Re–Os dating of molybdenite. Mineralium Deposita, 41, 33–45.

Hsu, Y.J., Zajacz, Z., Ulmer, P., Heinrich, C.A. (2017) Copper partitioning between silicate melts and amphibole: Experimental insight into magma evolution leading to porphyry copper ore formation. Chemical Geology, 448, 151-163.

Huang, M.L., Bi, X.W., Richards, J. P., Hu, R.Z., Xu, L.L., Gao, J.F., Zhu, J.J. and Zhang, X.C. (2019) High water contents of magmas and extensive fluid exsolution during the formation of the Yulong porphyry Cu-Mo deposit, eastern Tibet. Journal of Asian Earth Sciences, 176, 168-183.

Imai, A. (2002) Metallogenesis of porphyry Cu deposits of the western Luzon arc, Philippines: K-Ar ages, SO_3 contents of microphenocrystic apatite and significance of intrusive rocks. Resource Geology, 52, 147–161.

Imai, A. (2004) Variation of Cl and SO_3 contents of microphenocrystic apatite in intermediate to silicic igneous rocks of Cenozoic Japanese island arcs: implications for porphyry Cu metallogenesis in the Western Pacific Island arcs. Resource Geology 54, 357–372.

Irvine, I.N., and Baragar, W.R.A., (1971) A guide to the chemical classification of the common

762 volcanic rocks. Canadian journal of earth sciences 8, 523-548.

763 Isnard, H., Brennetot, R., Caussignac, C., Caussignac, N., and Chartier, F. (2005). Investigations
764 for determination of Gd and Sm isotopic compositions in spent nuclear fuels samples by MC
765 ICPMS. International Journal of Mass Spectrometry, 246, 66-73.

766 Jahnke, R.A. (1984) The synthesis and solubility of carbonate fluorapatite. American Journal of
767 Science 284, 58–78.

768 Jégo, S., and Pichavant, M. (2012) Gold solubility in arc magmas: Experimental determination of
769 the effect of sulfur at 1000°C and 0.4GPa. Geochimica et Cosmochimica Acta, 84, 560-592.
770 Jenner, F.E., O'Neill, H.S.C., Arculus, J.R., and Mavrogenes, J.A. (2010) The Magnetite crisis in
771 the evolution of arc-related magmas and the initial concentration of Au, Ag and Cu. Journal
772 of Petrology, 51, 2445-2464.

773 Johnston, A.D., and Schwab, B.E. (2004) Constraints on clinopyroxene/melt partitioning of REE,
774 Rb, Sr, Ti, Cr, Zr, and Nb during mantle melting: First insights from direct peridotite melting
775 experiments at 1.0 GPa. Geochimica et Cosmochimica Acta, 68, 4949-4962.

776 Jugo, P.J., and Candela, P.A. (1999) Magmatic sulfides and Au:Cu ratios in porphyry deposits : an
777 experimental study of copper and gold partitioning at 850°C, 100 MPa in a haplogranitic
778 melt-pyrrhotite-intermediate solid solution-gold metal assemblage, at gas saturation. Lithos,
779 46, 573-589.

780 Jugo, P. J., Luth, R. W., and Richards, J.P. (2005) Experimental data on the speciation of sulfur as
781 a function of oxygen fugacity in basaltic melts. Geochimica et Cosmochimica Acta, 69,
782 497-503.

783 Le Roux, V., Dasgupta, R., and Lee C.T.A. (2015) Recommended mineral-melt partition
784 coefficients for FRTEs (Cu), Ga, and Ge during mantle melting. American Mineralogist, 100,
785 2533-2544.

786 Lerchbaumer, L., and Audėtat, A. (2013) The metal content of silicate melts and aqueous fluids in
787 subeconomically Mo mineralized granites: implications for porphyry Mo genesis. Economic

Geology, 108, 987–1013.

Li, J.X., Qin, K.Z., Li, G.M., Evans, N.J., Zhao, J.X., Yue, Y.H., and Xie, J. (2018) Volatile variations in magmas related to porphyry Cu-Au deposits: Insights from amphibole geochemistry, Duolong district, central Tibet. Ore Geology Reviews, 95, 649-662.

Li, S., Yang, X.Y., Huang, Y., and Sun, W.D. (2014) Petrogenesis and mineralization of the Fenghuangshan skarn Cu–Au deposit, Tongling ore cluster field, Lower Yangtze metallogenic belt. Ore Geology Reviews, 58, 148-162.

Li, Y., and Audétat A. (2012) Partitioning of V, Mn, Co, Ni, Cu, Zn, As, Mo, Ag, Sn, Sb, W, Au, Pb, and Bi between sulfide phases and hydrous basanite melt at upper mantle conditions. Earth and Planetary Science Letters, 355-356, 327-340.

Li, Y. and Audétat, A. (2013) Gold solubility and partitioning between sulfide liquid, monosulfide solid solution and hydrous mantle melts: Implications for the formation of Au-rich magmas and crust–mantle differentiation. Geochimica et Cosmochimica Acta, 118, 247-262.

Li, Z.X., and Li, X.H. (2007) Formation of the 1300-km-wide intracontinental orogen and postorogenic magmatic province in Mesozoic South China: A flat-slab subduction model. Geology, 35, 179-182.

Liu, X., Xiong, X., Audétat, A., Li, Y. (2015) Partitioning of Cu between mafic minerals, Fe–Ti oxides and intermediate to felsic melts. Geochimica et Cosmochimica Acta, 151, 86-102.

Liu, Y.S., Hu, Z.C., Gao, S., Gunther, D., Xu, J., Gao, C.G., and Chen, H.H. (2008) In situ analysis of major and trace elements of anhydrous minerals by LA-ICP-MS without applying an internal standard. Chemical Geology, 257, 34–43.

Liu, Z.F., Shao, Y.J., Wang, C., and Liu, Q.Q. (2019) Genesis of the Dongguashan skarn Cu-(Au) deposit in Tongling, Eastern China: Evidence from fluid inclusions and H-O-S-Pb isotopes. Ore Geology Reviews, 104, 462-476.

London, D., Wolf, M.B., Morgan VI, G.B., and Garrido, M.G. (1999) Experimental silicate-phosphate equilibria in peraluminous granitic magmas, with a case study of

Albuquerque batholith at Tres Arroyos, Badajoz, Spain. Journal of Petrology, 40, 215–240.

Lu, S.M., Xu, X.C., Xie, Q.Q., Lou, J.W., Chu, G.Z., and Xiong, Y.P. (2007) Chemical and stable isotope geochemical characteristics of ore-forming fluid of the Shizishan copper and gold ore-field, Tongling, China. Acta Petrologica Sinica, 23, 177-184 (in Chinese with English abstract).

Mallmann, G., and O'Neill, H.S.C. (2009) The crystal/melt partitioning of V during mantle melting as a function of oxygen fugacity compared with some other elements (Al, P, Ca,Sc, Ti, Cr, Fe, Ga,Y, Zr and Nb). Journal of Petrology, 50, 1765-1794.

Maniar, P.D., and Piccoli, P.M. (1989) Tectonic discrimination of granitoids. Bulletin of the Geological Society of America, 101, 635.

Mao, M., Rukhlov, A.S., Rowins, S.M., Spence, J., and Coogan, L.A. (2016) Apatite trace element compositions: a robust new tool for mineral exploration. Economic Geology, 111, 1187-1222.

McInnes, B.I., McBride, J.S., Evans, N.J., Lambert, D.D., and Andrew, A.S. (1999) Osmium isotope constraints on ore metal recycling in subduction zones. Science, 286, 512-516.

Mercer, C.N., Watts, K.E., and Gross, J. (2020) Apatite trace element geochemistry and cathodoluminescent textures—A comparison between regional magmatism and the Pea Ridge IOAREE and Boss IOCG deposits, southeastern Missouri iron metallogenic province, USA. Ore Geology Reviews, 116, 103129.

Meinert, L.D., Dipple, G.M., and Nicolescu, S. (2005) World skarn deposits. Economic Geology, 100th Anniversary Volume, 299-336.

Miles, A.J., Graham, C.M., Hawkesworth, C.J., Gillespie, M.R., Hinton, R.W., Bromiley, G.D., and EMMAC. (2014) Apatite: A new redox proxy for silicic magmas? Geochimica et Cosmochimica Acta, 132, 101-119.

Moune, S., Holtz, F., and Botcharnikov, R.E. (2009) Sulphur solubility in andesitic to basaltic melts: implications for Hekla volcano. Contributions to Mineralogy and Petrology, 157, 691-707.

840 Mungall, J.E., and Brenan, J.M. (2014) Partitioning of platinum-group elements and Au between
841 sulfide liquid and basalt and the origins of mantle-crust fractionation of the chalcophile
842 elements. Geochimica et Cosmochimica Act, 125, 265-289.

843 Myers, J., and Eugster, H.P. (1983) The System Fe-Si-O: Oxygen Buffer Calibrations to 1500K.
844 Contributions to Mineralogy and Petrology, 82, 75-90.

845 Nardi, L.V.S., Formoso, M.L.L., Müller, I.F., Fontana, E., Jarvis, K., and Lamarão, C. (2013)
846 Zircon/rock partition coefficients of REEs, Y, Th, U, Nb, and Ta in granitic rocks: Uses for
847 provenance and mineral exploration purposes. Chemical Geology, 335, 1-7.

848 Palma, G., Barra, F., Reich, M., Valencia, V., Simon, A.C., Vervoort, J., Leisen, M., and Romero,
849 R. (2019) Halogens, trace element concentrations, and Sr-Nd isotopes in apatite from iron
850 oxide-apatite (IOA) deposits in the Chilean iron belt: Evidence for magmatic and
851 hydrothermal stages of mineralization. Geochimica et Cosmochimica Acta, 246, 515-540.

852 Pan, Y., and Dong, P. (1999) The lower Changjiang (Yangtze River) metallogenic belt, eastern
853 central China : intrusion- and wall rock-hosted Cu-Fe-Au, Mo, Zn, Pb, Ag deposits. Ore
854 Geology Reviews, 15, 177-242.

855 Pan, Y., and Fleet, M.E. (2002) Compositions of the apatite group minerals: substitution
856 mechanisms and controlling factors. Reviews in Mineralogy & Geochemistry, 48, 13–49.

857 Parat, F., Holtz, F., and Klügel, A., (2011) S-rich apatite-hosted glass inclusions in xenoliths from
858 La Palma: Constraints on the volatile partitioning in evolved alkaline magmas: Contributions
859 to Mineralogy and Petrology, 162, 463-478.

860 Patten, C., Barnes, S.J., Mathez, E.A., and Jenner, F.E. (2013) Partition coefficients of chalcophile
861 elements between sulfide and silicate melts and the early crystallization history of sulfide
862 liquid: LA-ICP-MS analysis of MORB sulfide droplets. Chemical Geology, 358, 170-188.

863 Peach, C.L., Mathez, E.A., and Keays, R.R. (1990) Sulfide melt-silicate melt distribution
864 coefficients for noble metals and other chalcophile elements as deduced from MORB:
865 Implications for partial melting. Geochimica et Cosmochimica Acta, 54, 3379-3389.

Peng, G., Luhr, J.F., and McGee, J.J. (1997) Factors controlling sulfur concentrations in volcanic apatite. American Mineralogist, 82, 1210-1224.

Pichavant, M., Montel, J.M., and Richard, L.R. (1992) Apatite solubility in peraluminous liquids: experimental data and an extension of the Harrison-Watson model. Geochimica et Cosmochimica Acta, 56, 3855–3861.

Piccoli, P.M., and Candela, P.A. (1994) Apatite in felsic rocks: a model for the estimation of initial halogen concentrations in the Bishop Tuff (Long Valley) and Tuolumne intrusive suite (Sierra Nevada batholith) magmas. American Journal of Science, 294, 92–135.

Piccoli, P.M., and Candela, P.A. (2002) Apatite in igneous systems. Reviews in Mineralogy & Geochemistry, 48, 255–292.

Qian, L., Wang, Y., Xie, J.C., and Sun, W.D. (2019) The Late Mesozoic granodiorite and polymetallic mineralization in southern Anhui Province, China: A perspective from apatite geochemistry. Solid Earth Sciences, 4,178-189.

Ramos, F. C., Wolff, J. A., and Tollstrup, D. L. (2004). Measuring $^{87}Sr/^{86}Sr$ variations in minerals and groundmass from basalts using LA-MC-ICPMS. Chemical Geology, 211, 135-158.

Richards, J.P. (2009) Postsubduction porphyry Cu-Au and epithermal Au deposits: products of remelting of subduction-modified lithosphere. Geology, 37, 247-250.

Richards, J.P. (2015) The oxidation state, and sulfur and Cu contents of arc magmas: implications for metallogeny. Lithos, 233, 27-45.

Richards, J.P. and Şengör, A.M.C. (2017) Did Paleo-Tethyan anoxia kill arc magma fertility for porphyry copper formation?. Geology, 45, 591-594.

Rittmann, A. (1957) On the serial character of igneous rocks. Egyptian Journal of Geology, 1, 23-48.

Rittmann, A. (1962) Volcanoes and Their Activity. New York, Interscience Publishers.

Rønsbo, J.G. (1989) Coupled substitutions involving REEs and Na and Si in apatites in alkaline

rocks from the IlÍmaussaq intrusion, South Greenland, and the petrological implications. American Mineralogist, 74, 896–901.

Rowins, S.M. (2000) Reduced porphyry copper-gold deposits: A new variation on an old theme. Geology 8, 167-180.

Rubatto, D., and Hermann, J. (2007) Experimental zircon/melt and zircon/garnet trace element partitioning and implications for the geochronology of crustal rocks. Chemical Geology, 241, 38-61.

Rudnick, R.L., and Gao, S. (2003) Composition of the continental crust. Treatise on Geochemistry, 3, 1-64.

Saunders, J.E., Pearson, N.J., O'Reilly, S.Y., and Griffin, W.L. (2018) Gold in the mantle: A global assessment of abundance and noredistribution processes. Lithos, 322, 376-391.

Sha, L.K., and Chappell, B.W. (1999) Apatite chemical composition, determined by electron microprobe and laser-ablation inductively coupled plasma mass spectrometry, as a probe into granite petrogenesis. Geochimica et Cosmochimica Acta, 63, 3861–3881.

Sillitoe, R.H. (2010) Porphyry Copper systems. Economic Geology, 105, 3-41.

Shao, Y.J., Peng, S.L., Lai, J.Q., Liu, L.M., Zhang, Y.Z., and Zhang, J.D. (2007) Identification of two types of mineralized intrusion in the Fenghuangshan copper deposit and analysis of their genesis. Acta Petrologica Sinica, 23, 2471-2482 (in Chinese with English abstract).

Stern, C.R., Funk, J.A., Skewes, M.A., and Arévalo, A. (2007) magmatic anhydrite in plutonic rocks at the El Teniente Cu-Mo deposit, Chile, and the role of sulfur-and copper-rich magmas in its formation. Economic Geology, 102, 1335-1344.

Streck, M.J., and Dilles, J.H. (1998) Sulfur evolution of oxidized arc magmas as recorded in apatite from a porphyry copper batholith. Geology, 26, 523–526.

Stormer, J.C., Pierson, M.L., and Tacker, R.C. (1993) Variation of F and Cl X-ray intensity due to anisotropic diffusion in apatite during electron microprobe analysis. American Mineralogist,

916 78, 641-648.

917 Sun, S.J., Yang, X.Y., Wang, G.J., Sun, W.D., Zhang, H., Li, C.Y., and Ding, X. (2019) In situ
918 elemental and Sr-O isotopic studies on apatite from the Xu-Huai intrusion at the southern
919 margin of the North China Craton: Implications for petrogenesis and metallogeny. Chemical
920 Geology, 510, 200-214.

921 Sun, S.S., and McDonough, W.F. (1989) Chemical and isotopic systematics of oceanic basalts:
922 implications for mantle composition and processes. Geological Society Special Publication,
923 42, 313–345.

924 Sun, W.D., Ding, X., Hu, Y.H., and Li, X.H. (2007) The golden transformation of the Cretaceous
925 plate subduction in the west Pacific. Earth and Planetary Science Letters, 262, 533-542.

926 Sun, W.D., Huang, R.F., Li, H., Hu, Y.B., Zhang, C.C., Sun, S.J., Zhang, L.P., Ding, X., Li, C.Y.,
927 Zartman, R.E., and Ling, M.X. (2015) Porphyry deposits and oxidized magmas. Ore Geology
928 Reviews, 65, 97-131.

929 Taylor, S.R. (1995) The geochemical evolution of the continental crust. Reviews of Geophysics,
930 33, 241-265.

931 Tepper, J.H., and Kuehner, S.M. (1999) Complex zoning in apatite from the Idaho batholith: a
932 record of magma mixing and intracrystalline trace element diffusion. American Mineralogist,
933 84, 581–595.

934 Tollari, N., Barnes S.J., Cox, R.A., Nabilb, H. (2008) Trace element concentrations in apatites
935 from the Sept-Îles Intrusive Suite, Canada -Implications for the genesis of nelsonites.
936 Chemical Geology, 252, 180-190.

937 Tu, W. (2014) Characteristics and genesis of the Chaoshan skarn gold deposit, Tongling, Anhui
938 Province. (PHD Thesis) China University of Geosciences (Beijing) (in Chinese with English
939 abstract).

940 Wang, Q., Wyman, D.A., Xu, J.F., Zhao, Z.H., Jian, P., Xiong, X.L., Bao, Z.W., Li, C.F., and Bai,
941 Z.H. (2006) Petrogenesis of Cretaceous adakitic and shoshonitic igneous rocks in the Luzong

942 area, Anhui Province (eastern China): Implications for geodynamics and Cu-Au
943 mineralization. Lithos, 89, 424-446.

944 Wang, C.S., Wu, C.L., Zheng, K., Wu, D., Shan, S.F., Li, X., and Gu, Q.D. (2018) Ore-forming
945 ages and sources of metallogenic materials of Fenghuangshan ore field in Tongling. Mineral
946 Deposits, 37, 1195-1216 (in Chinese with English abstract).

947 Wang, H., Zhang, Y., Chu, Y., Ma, H., Li, Y., Wu, D., Du, B., and Wei, Q. (2016) Disposable
948 competitive-type immunoassay for determination of aflatoxin B1 via detection of copper ions
949 released from Cu-apatite. Talanta, 147, 556-560.

950 Wang, J.Z., Li, J.W., Zhao, X.F., Ma, C.Q., Qu, W.J., and Du, A.D. (2008a) Re-Os Dating of
951 Pyrrhotite from the Chaoshan Gold Skarn, Eastern Yangtze Craton, Eastern China.
952 International Geology Review, 50, 392-406.

953 Wang, J.Z., Li, J.W., Zhao, X.F., Qian, Z.Z., and Ma, C.Q. (2008b) Genesis of the Chaoshan gold
954 deposit and its host intrusion, Tongling area: Constraints from $^{40}Ar/^{39}Ar$ ages and elemental
955 and Sr-Nd-O-C-S isotope geochemistry. Acta Petrologica Sinica, 24, 1875-1888 (in Chinese
956 with English abstract).

957 Wang, S.W., Zhou, T.F., Yuan, F., Fan, Y. , Zhang, L.J., and Song, Y.L. (2015) Petrogenesis of
958 Dongguashan skarn-porphyry Cu-Au deposit related intrusion in the Tongling district, eastern
959 China: Geochronological, mineralogical, geochemical and Hf isotopic evidence. Ore Geology
960 Reviews, 64, 53-70.

961 Wang, Y.B., Liu, D.Y., Zeng, P.S., Yang, Z.S., and Tian, S.H. (2004) SHRIMP U-Pb
962 geochronology of pyroxene diorite in the Chaoshan gold deposit and its geological
963 significance. Acta Geoscientica Sinica, 25, 423-427 (in Chinese with English abstract).

964 Warner, S., Martin, R.F., Abdel-Rahman, A.M., and Doig, R. (1998) Apatite as a monitor of
965 fractionation, degassing, and metamorphism in the Sudbury igneous complex, Ontario.
966 Canadian Mineralogist,, 36, 981–999.

967 Watson, E.B. (1979) Apatite saturation in basic to intermediate magmas. Geophysical Research

968 Letters, 6, 937–940.

969 Watson, E.B. (1980) Apatite and phosphorus in mantle source regions: an experimental study of
970 apatite/melt equilibria at pressures to 25 kbar. Earth and Planetary Science Letters, 51,
971 322–335.

972 Webster, J.D. (2004) The exsolution of magmatic hydrosaline chloride liquids. Chemical Geology,
973 210, 33-48.

974 Williams-Jones, A.E., Candela, P.A., and Piccoli, P.M. (1995) The partitioning of copper between
975 silicate melts and two-phase aqueous fluids: An experimental investigation at 1 Kbar, 800°C
976 and 0.5 Kbar, 850°C. Contributions to Mineralogy and Petrology, 121, 388-399

977 Wolf, M.B., and London, D. (1994) Apatite dissolution into peraluminous haplogranite melt: an
978 experimental study of solubilities and mechanisms. Geochimica et Cosmochimica Acta, 58,
979 4127–4145.

980 Wolf, M.B., and London, D. (1995) Incongruent dissolution of REE-and Sr-rich apatite in
981 peraluminous granitic liquids: differential apatite, monazite, and xenotime solublities during
982 anatexis. American Mineralogist, 80, 765–775.

983 Xie, J.C., Yang, X.Y., and Sun, W.D. (2012) Early Cretaceous dioritic rocks in the Tongling region,
984 eastern China: Implications for the tectonic settings. Lithos, 150, 49-61.

985 Xie, J.C. (2008) The diagenesis and metallogenesis research of Mesozoic magmatic rocks in
986 Tongling region, Anhui Province. (PHD Thesis) University of Science and Technology of
987 China (in Chinese with English abstract).

988 Xu, J.F., Shinjo, R., Defant, M.J., Wang, Q., and Rapp, R.P. (2002) Origin of Mesozoic adakitic
989 intrusive rocks in the Ningzhen area of east China: partial melting of delaminated lower
990 continental crust. Geology, 30, 1111-1114.

991 Xu, L.L., Bi, X.W., Hu, R.Z., Tang, Y.Y., Wang, X.S., Huang, M.L., Wang, Y.J., Ma, R., and Liu,
992 G. (2019) Contrasting whole-rock and mineral compositions of ore-bearing (Tongchang) and
993 ore-barren (Shilicun) granitic plutons in SW China: Implications for petrogenesis and ore

994 genesis. Lithos, 336-337, 54-66.

995 Xu, X.C., Lu, S.M., Xie, Q.Q., Bo, L., and Chu, G.Z., (2008) SHRIMP zircon U-Pb dating for the
996 magmatic rocks in Shizishan ore-field of Tongling, Anhui Province, and its geological
997 implications. Acta Geologica Sinica, 82, 501-509 (in Chinese with English abstract).

998 Yang, X.N., Xu, Z.W., Gao, G., Lu, X.C., Liu, S.M., and Li, H.Y. (2008) Fluid inclusion studies of
999 the Chaoshan gold deposit in Tongling, Anhui Province, China. Acta Petrologica Sinica, 24,
1000 1889-1899 (in Chinese with English abstract).

1001 Yang, Y. H., Wu, F.Y., Yang, J. H., Chew, D.M., Xie, L. W., Chu, Z. Y., Zhang,Y.B., and Huang, C.
1002 (2014). Sr and Nd isotopic compositions of apatite reference materials used in U–Th–Pb
1003 geochronology. Chemical Geology, 385, 35-55.

1004 Zajacz, Z., Candela, P. A., Piccoli, P. M., Wälle, M., and Sanchez-Valle, C. (2012) Gold and
1005 copper in volatile saturated mafic to intermediate magmas: Solubilities, partitioning, and
1006 implications for ore deposit formation: Geochimica et Cosmochimica Acta, 91, 140-159.

1007 Zen, E. (1986) Aluminum enrichment in silicate melts by fractional crystallization: some
1008 mineralogic and petrographic constraints. Journal of Petrology, 27, 1095-1117.

1009 Zhang, D., and Audétat, A. (2017) What Caused the Formation of the Giant Bingham Canyon
1010 Porphyry Cu-Mo-Au Deposit? Insights from Melt Inclusions and Magmatic Sulfides.
1011 Economic Geology, 112, 221-244.

1012 Zhou, X.M., Sun, T., Shen, W.Z., Shu, L.S., and Niu, Y.L. (2006) Petrogenesis of Mesozoic
1013 granitoids and volcanic rocks in South China: a response to tectonic evolution. Episodes, 29,
1014 26-33.

1015 Zhu, J.J., Richards, J.P., Rees, C., Creaser, R.,. DuFrane, A., Locock,A., Petrus, J.A., and Lang, J.
1016 (2018) Elevated magmatic sulfur and chlorine contents in ore-forming magmas at the Red
1017 Chris porphyry Cu-Au deposit, Northern British Columbia, Canada. Economic Geology, 113,
1018 1047-1075.

1019

Figures

Figure 1 Regional geological map of the research area (modified from Liu et al., 2019)

Figure 2 Simplified geological maps for the Chaoshan, Dongguashan and Hucun intrusions (a), and the Xinwuli intrusion (b)

Figure 3 The modes of occurrence of apatite in the rock samples from the selected intrusions. Ap = apatite; Bt =biotite; Hbl = hornblende; Pl=plagioclase; Hbl = hornblende; Pl = plagioclase; Qtz = quartz; Ttn = titanite.

Figure 4 (Na_2O+K_2O) vs. SiO_2 diagram (Irvine and Baragar, 1971) (a); A/NK vs. A/CNK diagram (Maniar and Piccoli 1989) for the Chaoshan, Hucun, Dongguashan, and Xinwuli intrusions (b); Chondrite-normalized trace-element diagrams (c) and REE diagrams (d)for the selected intrusions. Data are listed in Supplementary Materials 1. The chondrite values are from Sun and McDonough (1989)

Figure 5 Plots of CaO vs. MnO (a), CaO vs. Na_2O (b), Na_2O vs. SO_3 (c), CaO vs. REE (d), CaO vs. P_2O_5 (e), F vs.Cl (f), Na_2O vs. REE (g), and Y vs. REE (h) in apatite from the selected intrusions

Figure 6 Chondrite-normalized REE patterns for apatite from the selected intrusions. Data are listed in Supplementary Materials 2. The chondrite values are from Sun and McDonough (1989)

Figure 7 The molar ratio of Ca/100-Mn-Fe, Ca/100-Mn-Na and fluorapatite (FAP)- chlorapatite (CAP)-hydroxylapatite (HAP) in apatite from the selected intrusions. The base map is from Piccoli and Candela (2002). The calculated method on the mole fraction of FAP, CAP, and HAP is from Piccoli and Candela (2002).

Figure 8 Plots of Sr vs. δEu (a), Ga vs. Sr (b), V vs. Cr (c), Ce/La vs. Nd/Yb (d) in apatite from the selected intrusions and the estimated magma oxygen fugacity from Table 1 (c)

Figure 9 Plots of Cl vs. SO_3 , F vs. SO_3 and Cl vs. F/Cl in apatite from the selected intrusions

Figure 10 Plots of F/Cl vs. Sr (a), and mole fraction of chloraptite vs. hydroxylapatite (b) in apatite from the selected intrusions

1045 Figure 11 Plots of Cl vs. Cu and SO_3 vs.Cu in apatite from the selected intrusions

1046 Figure 12 Plots of average $(^{87}Sr/^{88}Sr)_i$ vs. average εNd(t) in apatite from the selected intrusions

This is the peer-reviewed, final accepted version for American Mineralogist, published by the Mineralogical Society of America.
The published version is subject to change. Cite as Authors (Year) Title. American Mineralogist, in press.
DOI: https://doi.org/10.2138/am-2021-7497. http://www.minsocam.org/

Table 1. Estimation of magmatic oxygen fugacity and the contents of S, Cl and F using apatite compositions

Intrusion	Average apatite Mn (ppm)	Average apatite SO_3 (ppm)	Average apatite F (wt.%)	Average apatite Cl (wt.%)	a: Average magmatic SO_3 content （ppm）	b: Average magmatic SO_3 content （ppm）	c: Average magmatic F content （ppm）	c: Average magmatic Cl content （ppm）	d: Zircon Ti temperature (℃)	e:△FMQ
Chaoshan	797	2834	2.44	0.45	116	1067	814	5568	957	+0.1
Xinwuli	279	560	2.89	0.11	27	23	963	1415	815	+3.8
Hucun	813	1747	2.76	0.32	58	24	919	3994	757	+3.9
Dongguashan	646	1977	2.52	0.33	67	69	839	4130	807	+3.2

a: Calculated equation of magmatic SO_3 content is from Peng et al. (1997): $\ln K_D\ (SO_3)_{apatite}/(SO_3)_{melt} = 21130/T - 16.2$

b: Calculated equation of magmatic SO_3 content is from Parat et al. (2011): SO_3 apatite (wt. %) = 0.157 × ln SO_3 glass (melt, wt %) + 0.9834

c: Partition coefficients of F and Cl are from Parat et al.(2011).D_{Cl} apatite/melt=0.8; D_F apatite/melt=30

d: Ti-in-zircon thermometry is from Ferry and Watson (2007): log (Ti in zircon ppm)=5.711±0.072-(4800±86)/T(K)-loga_{SiO2}+loga_{TiO2}. a_{SiO2} is equal to1.0 and a_{TiO2} is equal to 0.5. Apatite saturation temperature can not represent the temperature of massive crystallization of apatite in the intermediate magma (Piccoli and Candela, 2002). Instead, Ti-in-zircon thermometry could better reveal the temperature of early magma because this calculation can avoid the error caused by the use of whole-rock compositions as parameters to represent magmatic compositions

e: FMQ (fayalite-magnetite-quartz oxygen fugacity buffer) is from Myers and Eugster (1983); The calculated equation of oxygen fugacity using apatite Mn is

from Miles et al. (2014): log (fO_2) =-0.0022 ($\pm$0.0003) Mn(ppm)-9.75($\pm$0.46)

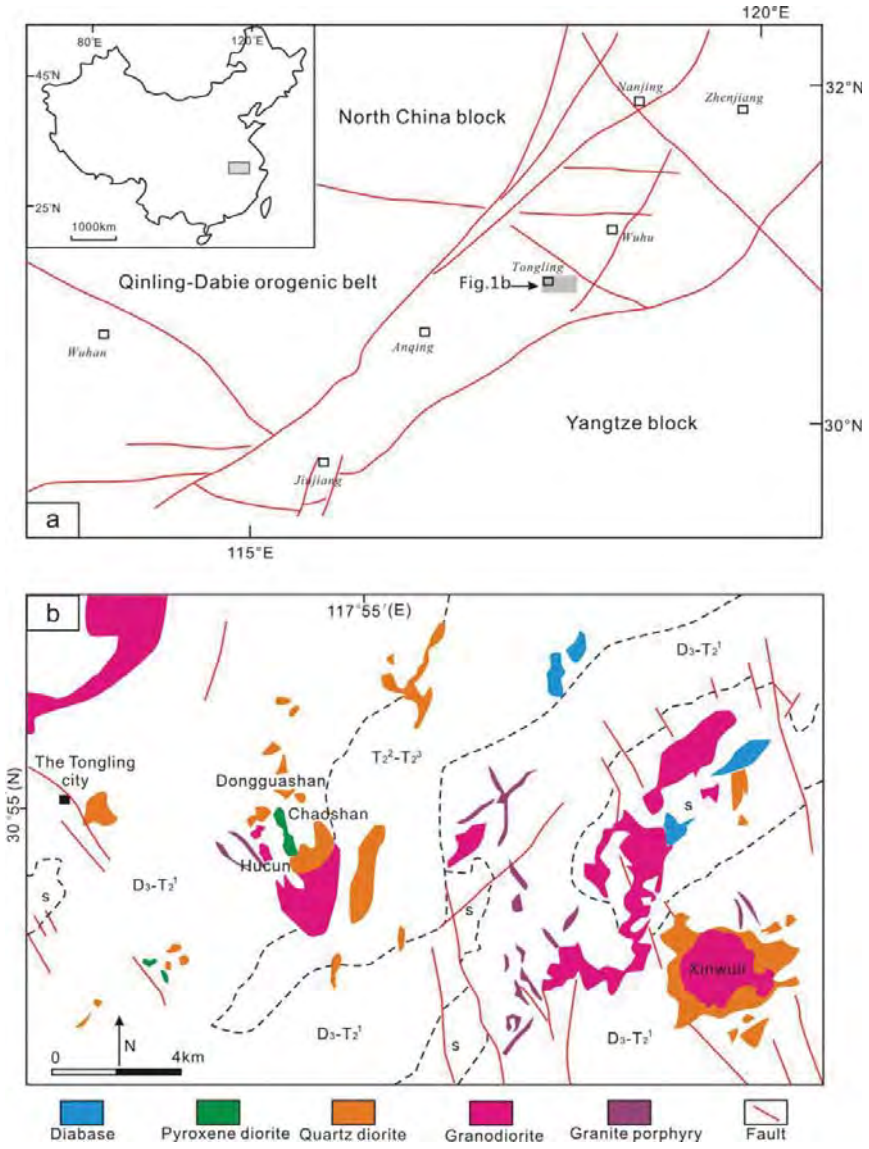

Figure. 1

This is the peer-reviewed, final accepted version for American Mineralogist, published by the Mineralogical Society of America.
The published version is subject to change. Cite as Authors (Year) Title. American Mineralogist, in press.
DOI: https://doi.org/10.2138/am-2021-7497. http://www.minsocam.org/

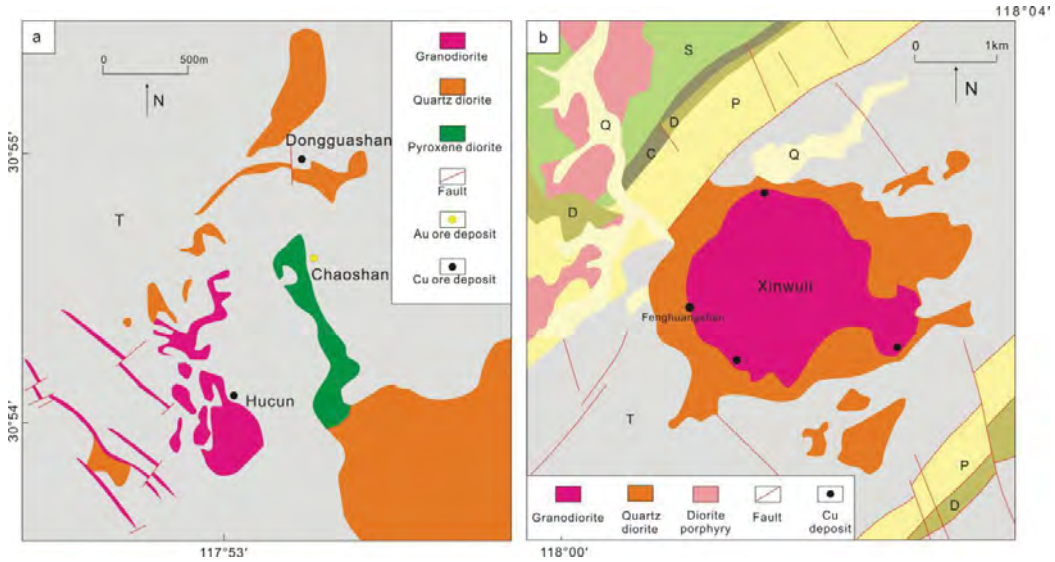

Figure. 2

This is the peer-reviewed, final accepted version for American Mineralogist, published by the Mineralogical Society of America.
The published version is subject to change. Cite as Authors (Year) Title. American Mineralogist, in press.
DOI: https://doi.org/10.2138/am-2021-7497. http://www.minsocam.org/

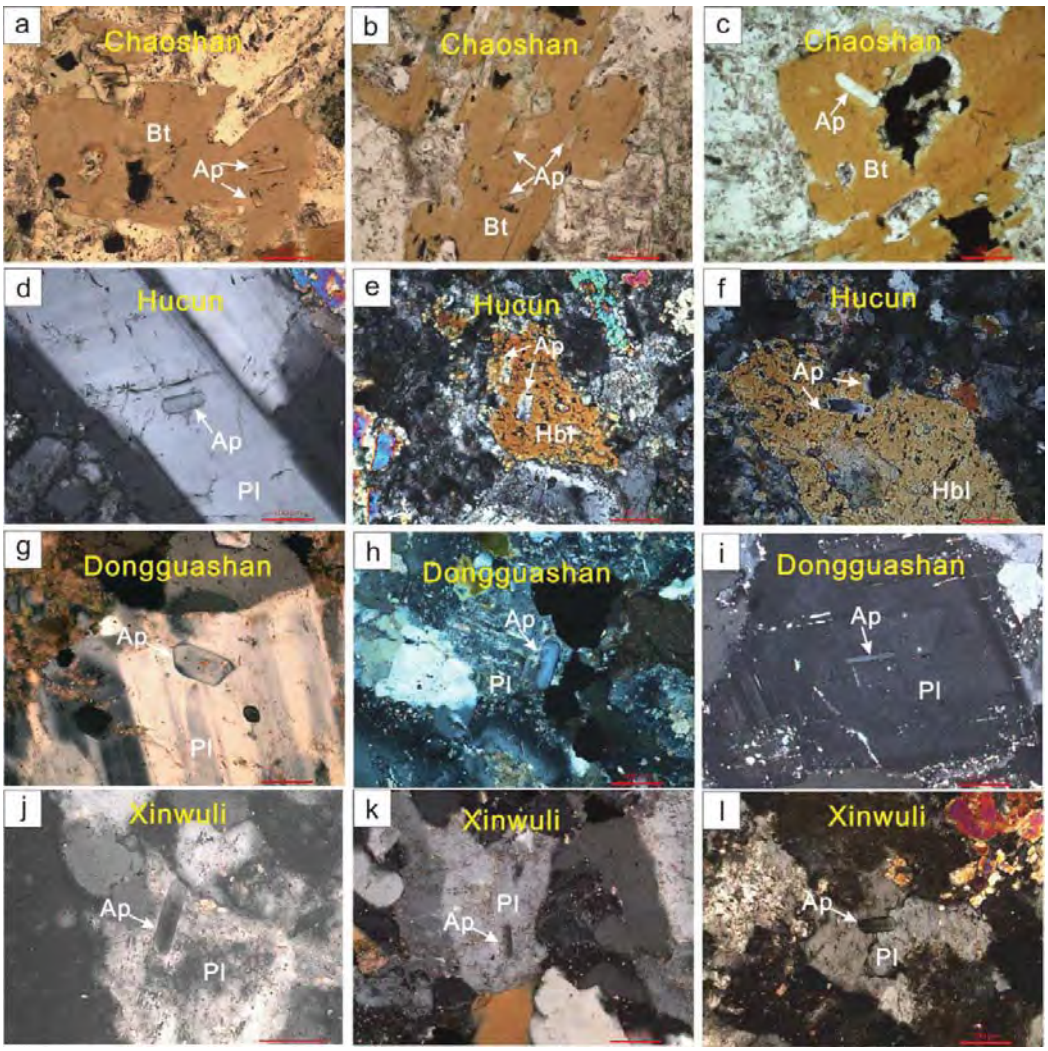

Figure. 3

This is the peer-reviewed, final accepted version for American Mineralogist, published by the Mineralogical Society of America.
The published version is subject to change. Cite as Authors (Year) Title. American Mineralogist, in press.
DOI: https://doi.org/10.2138/am-2021-7497. http://www.minsocam.org/

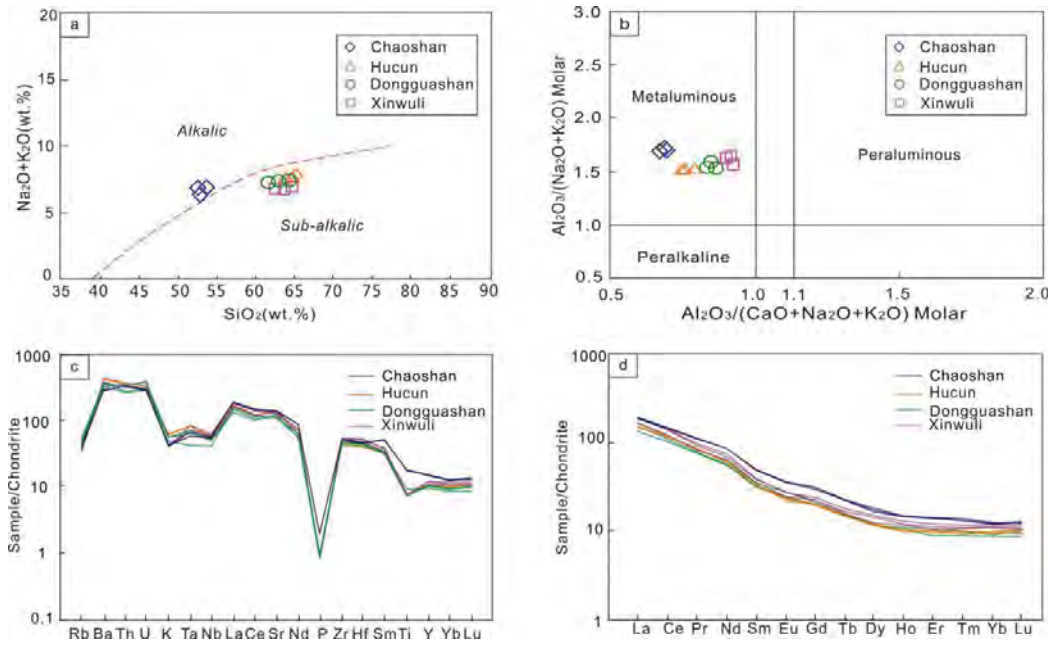

Figure. 4

This is the peer-reviewed, final accepted version for American Mineralogist, published by the Mineralogical Society of America.
The published version is subject to change. Cite as Authors (Year) Title. American Mineralogist, in press.
DOI: https://doi.org/10.2138/am-2021-7497. http://www.minsocam.org/

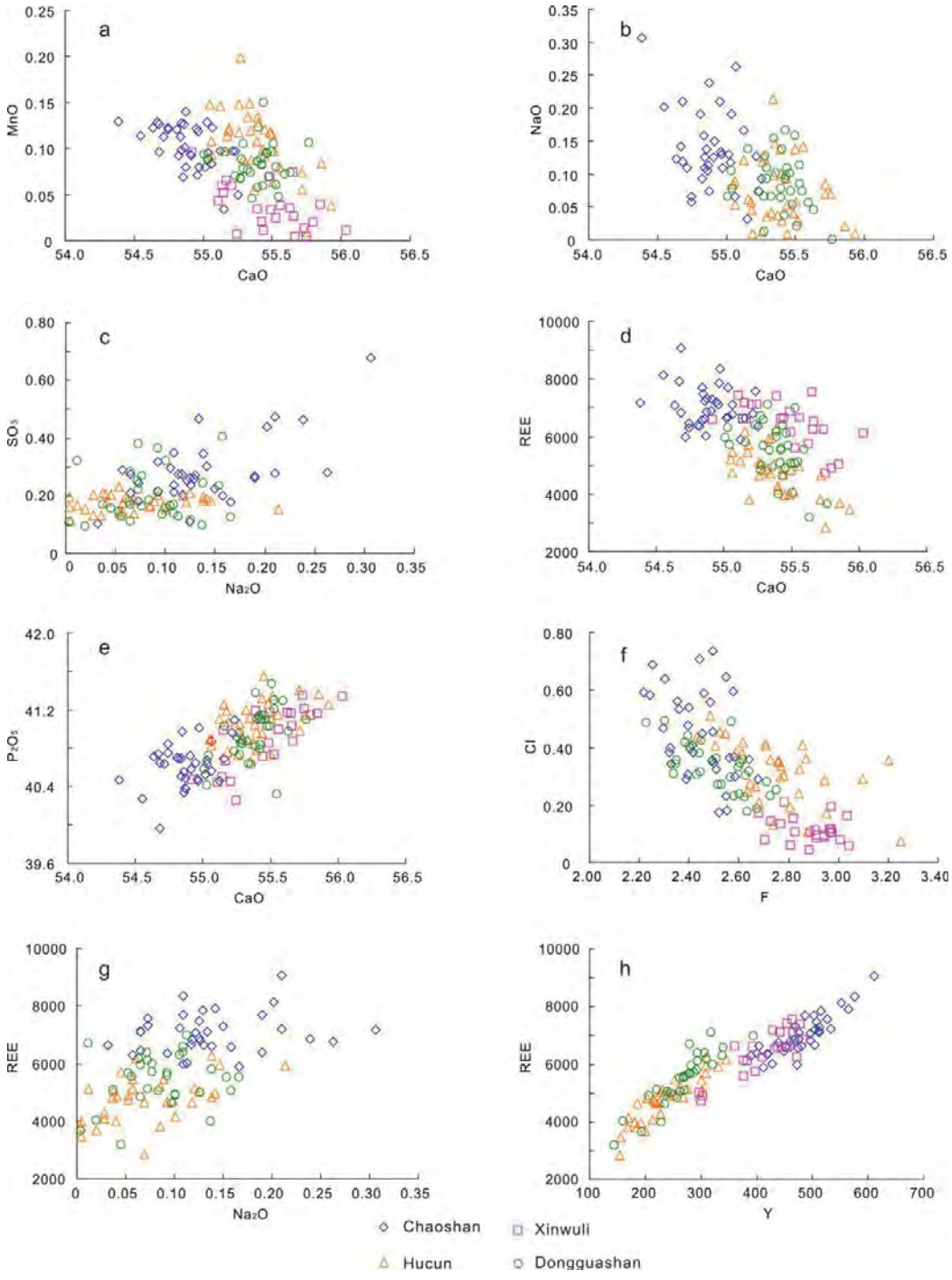

Figure. 5

This is the peer-reviewed, final accepted version for American Mineralogist, published by the Mineralogical Society of America.
The published version is subject to change. Cite as Authors (Year) Title. American Mineralogist, in press.
DOI: https://doi.org/10.2138/am-2021-7497. http://www.minsocam.org/

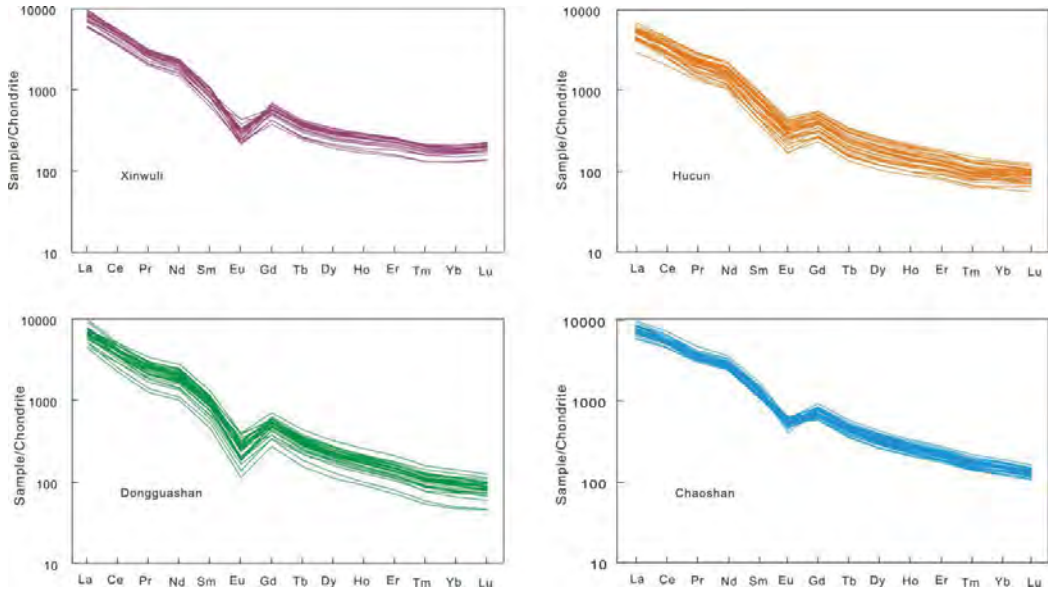

Figure .6

This is the peer-reviewed, final accepted version for American Mineralogist, published by the Mineralogical Society of America.
The published version is subject to change. Cite as Authors (Year) Title. American Mineralogist, in press.
DOI: https://doi.org/10.2138/am-2021-7497. http://www.minsocam.org/

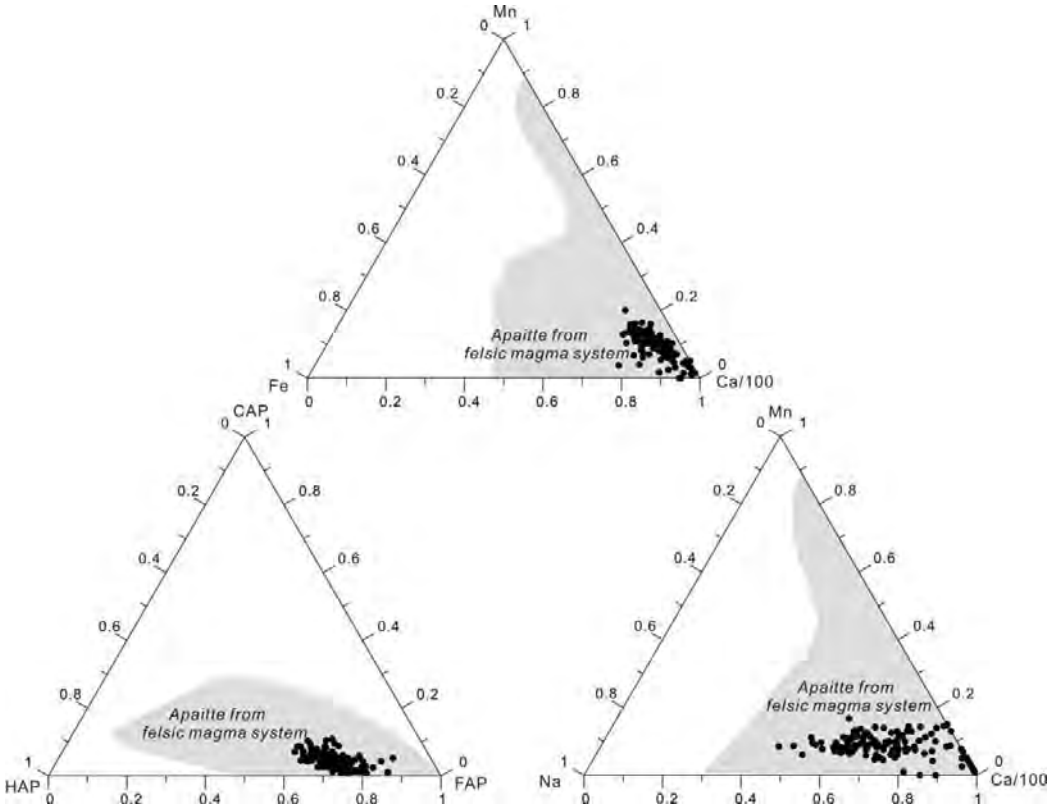

Figure .7

This is the peer-reviewed, final accepted version for American Mineralogist, published by the Mineralogical Society of America.
The published version is subject to change. Cite as Authors (Year) Title. American Mineralogist, in press.
DOI: https://doi.org/10.2138/am-2021-7497. http://www.minsocam.org/

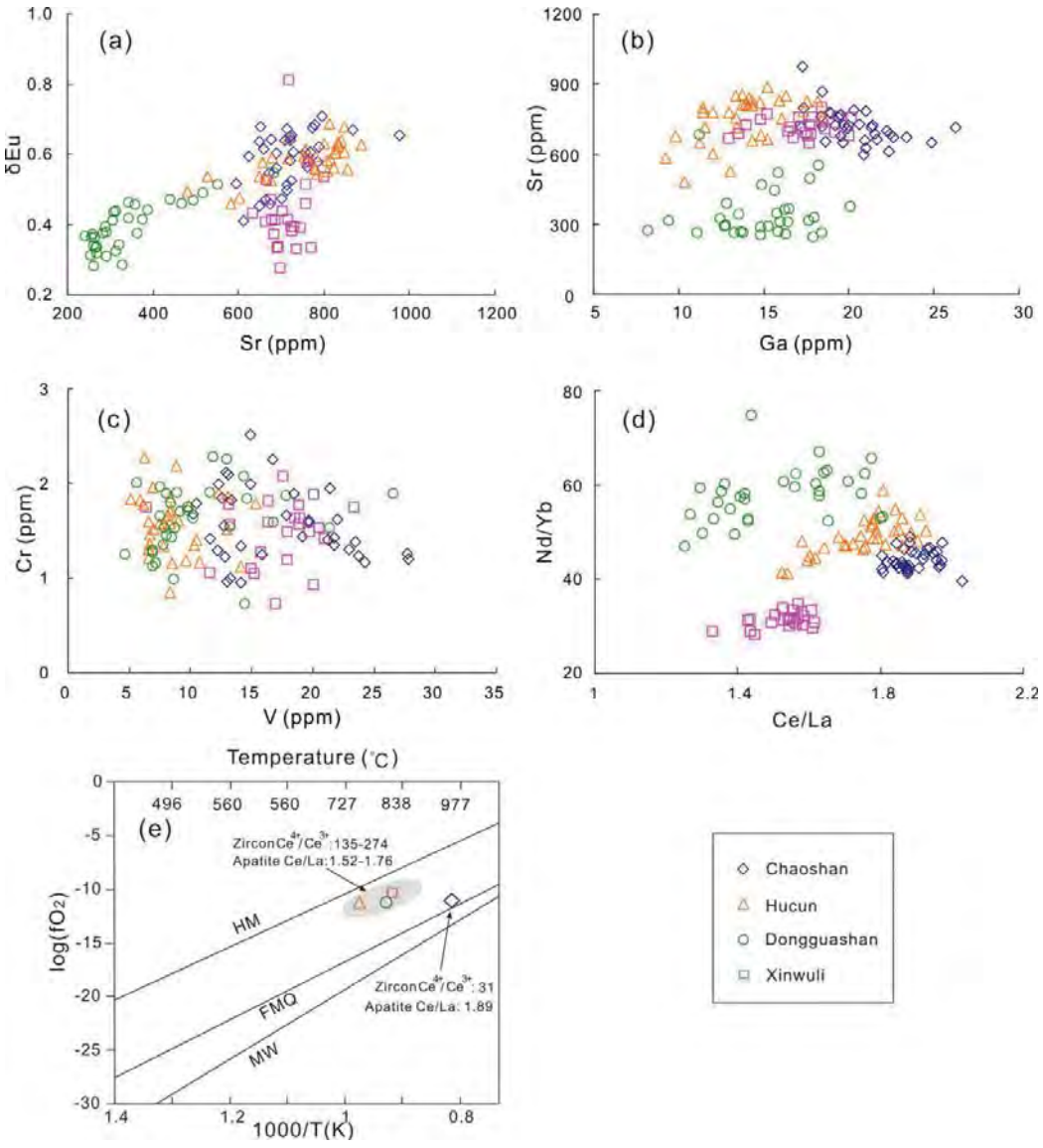

Figure. 8

This is the peer-reviewed, final accepted version for American Mineralogist, published by the Mineralogical Society of America.
The published version is subject to change. Cite as Authors (Year) Title. American Mineralogist, in press.
DOI: https://doi.org/10.2138/am-2021-7497. http://www.minsocam.org/

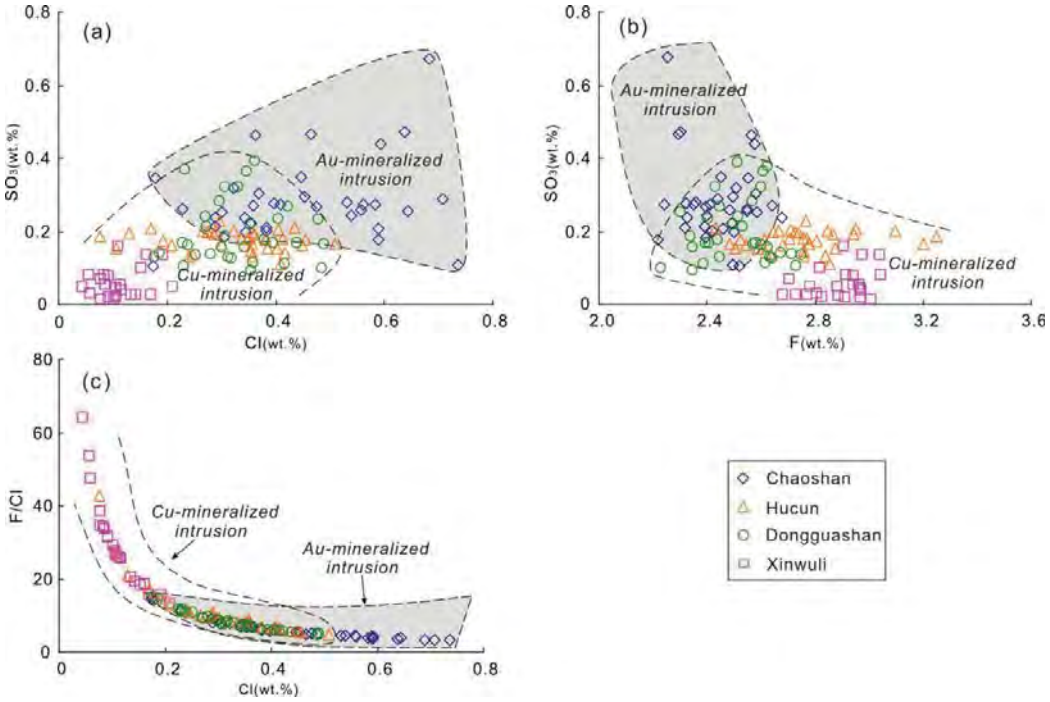

Figure. 9

This is the peer-reviewed, final accepted version for American Mineralogist, published by the Mineralogical Society of America.
The published version is subject to change. Cite as Authors (Year) Title. American Mineralogist, in press.
DOI: https://doi.org/10.2138/am-2021-7497. http://www.minsocam.org/

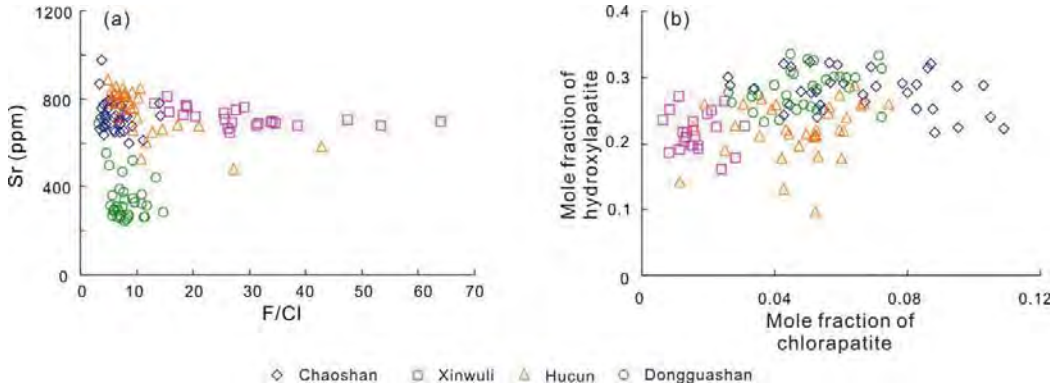

Figure. 10

This is the peer-reviewed, final accepted version for American Mineralogist, published by the Mineralogical Society of America.
The published version is subject to change. Cite as Authors (Year) Title. American Mineralogist, in press.
DOI: https://doi.org/10.2138/am-2021-7497. http://www.minsocam.org/

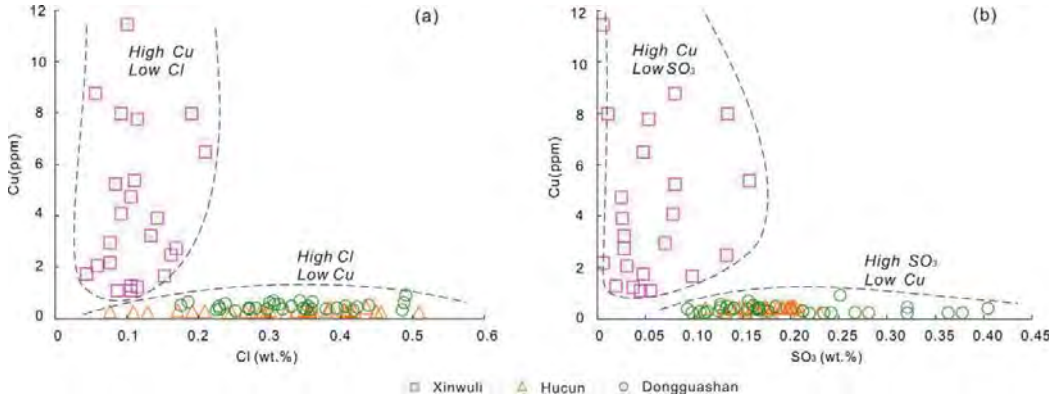

Figure. 11

This is the peer-reviewed, final accepted version for American Mineralogist, published by the Mineralogical Society of America.
The published version is subject to change. Cite as Authors (Year) Title. American Mineralogist, in press.
DOI: https://doi.org/10.2138/am-2021-7497. http://www.minsocam.org/

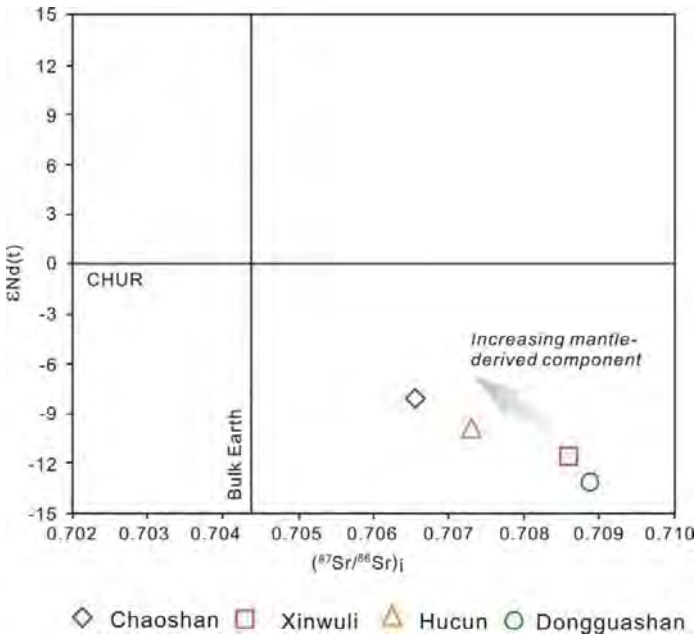

Figure. 12